47th AIAA Aerospace Sciences Meeting Including The New Horizons Forum and Aerospace Exposition
5 - 8 January 2009, Orlando, Florida

AIAA 2009-942

Effect of porous coating and its location on hypersonic boundary layer waves

Xiaowen Wang [*] **and Xiaolin Zhong** [†]
Mechanical and Aerospace Engineering Department
University of California, Los Angeles, California 90095

Abstract

In this paper, effect of porous coating and its location on the spatial developments of mode S and mode F in a Mach 5.92 flat-plate boundary layer is investigated by linear stability theory (LST) and direct numerical simulation (DNS). The current study is motivated by Fedorov et al.'s experimental and theoretical studies of the effect of an ultrasonically absorptive coating on hypersonic boundary-layer stability [1] and our previous numerical simulations on hypersonic boundary-layer stabilities [2, 3]. The mean flow is calculated by solving compressible Navier-Stokes equations with a combination of a fifth-order shock-fitting method and a second-order total variation diminishing (TVD) scheme. The stability characteristics of the hypersonic boundary layer is analyzed by LST. Stability simulations based on mean flow consist of three steps: 1. disturbances corresponding to a specific boundary layer wave (mode S or mode F) at a frequency of 100 kHz are introduced at the inlet of the computational domain to study its spatial development; 2. porous coating is used to investigate its effect on the spatial development of mode S and mode F; 3. multiple porous coatings are used to study the effect of porous coating location on the spatial development of mode S and mode F. The same theoretical model of porous coating as that in Fedorov et al.'s paper is used, i.e., porous coating is modelled by pressure perturbation related wall blowing-suction. For all the cases considered in current paper, porous coatings are located upstream of the corresponding synchronization point of mode S and mode F at $x_s^* = 0.33184$ m. The numerical results show that porous coating and its location have significant effects on the spatial developments of mode S and mode F. No matter which mode of mode S and mode F is introduced at the inlet, porous coating increases pressure perturbation amplitude downstream of the porous region. With the number of porous coatings increasing, pressure perturbation amplitude keeps increasing. In case of mode S, the effect of porous coating on mode S in porous region is not consistent. With the location of porous coating shifting from upstream to downstream, the effect of porous coating on mode S changes from destabilization to stabilization. In case of mode F, all cases show that mode F changes to mode S near the synchronization point and mode F is stabilized in porous region.

1 Introduction

Due to the fact that a turbulent boundary layer generates much higher shear stress and heat flux to the wall surface than a laminar boundary layer, the performance and thermal protection system of hypersonic transportation vehicles and re-entry vehicles are significantly affected by the transition of boundary-layer flows over vehicle surfaces. Controlling transition and maintaining a laminar boundary layer as long as possible results in better fuel efficiency, lower drag and heat flux.

In order to predict and control boundary-layer transition, extensive studies have been carried out to reveal transition mechanisms [4, 5, 6, 7, 8, 9]. It is recognized that the transition process of a boundary-layer flow strongly depends on the amplitude level of environmental perturbations [10, 11], which is schematically shown in Fig. 1. According to Reshotko's analysis [11], only the first three paths had relevance to external flows. In an environment of small amplitude perturbations, transition of the boundary-layer flow over a smooth surface generally consists of the following three stages (path 1):

---

[*] Postdoctoral Researcher,Mechanical and Aerospace Engineering Department, AIAA Member.

[†] Professor, Mechanical and Aerospace Engineering Department, AIAA Associate Fellow.

- Stage 1: Receptivity process during which small amplitude environmental disturbances enter the boundary layer and excite boundary-layer wave modes;
- Stage 2: Linear development or growth of unstable boundary-layer wave modes which can be predicted by solving the eigen-problem of the homogeneous linearized stability equations;
- Stage 3: Boundary-layer transition caused by non-linear breakdown and three-dimensional effects when the unstable wave modes reach certain amplitudes.

For high amplitude perturbations, transient growth provided a higher initial amplitude to eigenmode growth (path 2). On surface with stationary roughness elements, the strong transient growth of boundary-layer wave modes may directly lead to transition [10, 11] (path 3). All these transitions relating to high amplitude perturbations and transient growth are called bypass transition. In current paper, only small amplitude perturbations are considered. The undergoing path in this particular configuration is path 1. However the eigenmode growth of unstable boundary-layer wave is too weak to lead to transition.

In hypersonic boundary layers, two types of modes, mode S and mode F, are generally excited in receptivity process. These modes are given the names because they are tuned to slow and fast acoustic waves, respectively, in the limit of small Reynolds numbers. Mode F and mode S were first computed by Mack [12] for the compressible Blasius boundary layer. Mack found mode F to be stable, while mode S was found to be unstable and therefore more relevant in the transition process. Mode S constitutes both the first and second modes of Mack. The first mode is an inviscid instability wave, the counterpart of the Tollmien-Schlichting (T-S) waves at low-speed flows. Because compressible boundary-layer profiles contain an inflection point, the first mode begins to dominate with the Mach number increasing. The second mode belongs to a family of trapped acoustic modes, generally occurring for Mach numbers larger than 4. Once it is excited, the second mode is mode unstable than the first mode. According to the transition procedure, stabilizations of first mode and second mode are critical to transition control.

Techniques used to control laminar-turbulent transition can be divided into two types: passive control and active control. Passive control requires modification to the mean flow to inhibit the growth of boundary-layer modes, such as controlling mean surface temperature, modifying pressure gradient, and introducing localized steady surface suction. More passive control approaches were reviewed in Saric [13]. Active control aims to suppress the environmental disturbances. For example, the wave-like disturbances can be cancelled by introducing another wave of the same amplitude but opposite phase. Thomas [14] experimentally illustrated the concept of controlling boundary-layer transition by superimposing in the flow Tollmien-Schlichting waves that were of equal amplitude and antiphased to the disturbances. In all experiments, two electromagnetically excited vibrating ribbons were used to generate the instability waves in the flow, with the first ribbon working as an excitation source and the second one as an actuator. Both hot-wire surveys and flow visualization showed that it was possible to delay transition by appropriate adjustment of the phase and amplitude of the signal driving the second ribbon. Sturzebecher and Nitsche [15] showed that a sensor-actuator system combined with an adaptive control algorithm could successfully be used to achieve a powerful attenuation of naturally excited two-dimensional Tollmien-Schlichting (T-S) instabilities on an unswept wing. With a pure two dimensional control system, a local T-S wave was reduced in amplitude by about 90% . They also claimed that three-dimensional instabilities were successfully cancelled by means of a spanwise arrangement of sensors and actuators. Recently, Li and Gaster [16] numerically and experimentally investigated the control of spatially evolving three-dimensional instability waves in a flat-plate boundary layer with zero pressure gradient. They created the instability waves by computer-generated perturbations in a low-turbulence wind tunnel, then detected the oncoming disturbances and sent appropriate control signal to the downstream actuators to generate counteracting disturbances. They achieved good agreement between the experimental measurement and numerical predictions based on linear theory, which indicated that the growth of the three-dimensional instability waves could be inhibited by a simple control strategy.

Fedorov et al. [1] studied the effect of an ultrasonically absorptive coating (UAC) on hypersonic boundary-layer stability by experiment and theoretical analysis. Experiments were performed on a 7-degree half-angle sharp cone in a Mach 6 wind tunnel. Half-surface of the cone was solid and the other half-surface was covered by a porous coating. Both stability analysis and experimental results on two- and three-dimensional disturbances showed that the porous coating strongly stabilized the second mode and marginally destabilized the first mode. Since the first mode is spatially developed into the second mode downstream, destabilization of the first mode actually decreases the efficiency of the second mode stabilization. A straightforward way to avoid the destabilization of the first mode is to move the UAC coating further downstream to a location where the second mode is dominated. Based on previous numerical simulations on the receptivity of a Mach 8.0 flow to wall blowing-suction, Wang and Zhong [2] showed that the synchronization point of mode F and mode S played an important role in the excitation of mode S by wall blowing-suction. Mode S was strongly excited when the blowing-suction actuator was located upstream of the synchronization point. On the other hand, when the blowing-suction actuator was downstream of the synchronization point, there was a very weak excitation of mode S, despite the fact that the blowing-suction actuator was still within the unstable region of mode S. Such results indicate that the synchronization point may be the perfect location to start UAC coating. The accuracy of our simulations has been validated by a concurrent theoretical study carried out by Tumim, Wang, and Zhong [17] to compare the theoretical and numerical results of receptivity coefficients and to analyze the receptivity characteristics. The perturbation flow field downstream of the blowing-suction actuator was decomposed into boundary-layer wave modes with the help of the biorthogonal eigenfunction system. It was found that there was a good agreement between normal-mode amplitudes calculated with the help of the theoretical receptivity model and those obtained by projecting the numerical results onto the normal modes.

Recently, Wang and Zhong [3] preliminarily investigated the role of the synchronization point on stabilization of a Mach 5.92 flat-plate boundary layer using a porous coating. In our simulations, periodic wall blowing-suction disturbance was introduced near the leading edge to excite boundary-layer waves. Then porous coating was used near the synchronization point to stabilize boundary-layer waves. The numerical results showed that at the frequency of 100 kHz, porous coating destabilized boundary-layer waves when it was located upstream of the synchronization point and stabilized boundary-layer waves when it was located downstream of the synchronization point. These results indicated that the synchronization point plays an important role on the stabilization of the hypersonic boundary layer using porous coating. The most efficient way to stabilize boundary layer was to put porous coating downstream of the synchronization point. However, perturbations excited by wall blowing-suction consisted of mode F, mode S, and continuous waves, it was impossbile to study the effect of porous coating on the developments of mode F and mode S.

In this paper, effect of porous coating and its location on the spatial developments of mode S and mode F in a Mach 5.92 flat-plate boundary layer is investigated by linear stability theory (LST) and direct numerical simulation (DNS). The mean flow is calculated by solving compressible Navier-Stokes equations with a combination of a fifth-order shock-fitting method and a second-order total variation diminishing (TVD) scheme. The stability characteristics of the hypersonic boundary layer is analyzed by LST. Stability simulations based on mean flow consist of three steps: 1. disturbances corresponding to a specific boundary layer wave (mode S or mode F) at a frequency of 100 kHz are introduced at the inlet of the computational domain to study its spatial development; 2. porous coating is used to investigate its effect on the spatial development of mode S and mode F; 3. multiple porous coatings are used to study the effect of porous coating location on the spatial development of mode S and mode F. The same theoretical model of porous coating as that in Fedorov et al.'s paper is used, i.e., porous coating is modelled by pressure perturbation related wall blowing-suction. For all the cases considered in current paper, porous coatings are located upstream of the corresponding synchronization point of mode S and mode F at $x_s^* = 0.33184$ m.

2 Governing Equations and Numerical Methods

In the current numerical studies, a Mach 5.92 boundary layer over a flat plate as shown in Fig. 2 is considered. The flow is assumed to be thermally and calorically perfect. The governing equations for the simulation are the compressible Navier-Stokes equations in the conservative form, i.e.,

$$\frac{\partial \vec{U}^*}{\partial t^*} + \frac{\partial}{\partial x_1^*}(\vec{F}_{1i}^* + \vec{F}_{1v}^*) + \frac{\partial}{\partial x_2^*}(\vec{F}_{2i}^* + \vec{F}_{2v}^*) = 0 \tag{1}$$

where $\vec{U}^*$ is a column vector containing the conservative variables of mass, momentum, and energy, i.e.,

$$\vec{U}^* = \{\rho^*, \rho^* u_1^*, \rho^* u_2^*, e^*\}^{\mathrm{T}} \tag{2}$$

The superscript "$*$" represents dimensional variables. The flux vectors in Eq. (1) are divided into their inviscid and viscous components, because the two components are discretized with different schemes. The components, $\vec{F}_{1i}^*$ and

$\vec{F}_{2i}^*$, are inviscid flux whereas $\vec{F}_{1v}^*$ and $\vec{F}_{2v}^*$ are viscous flux components. The flux components can be expressed as

$$\vec{F}_{ji}^* = \begin{bmatrix} \rho^* u_j^* \\ \rho^* u_1^* u_j^* + p^* \delta_{1j} \\ \rho^* u_2^* u_j^* + p^* \delta_{2j} \\ u_j^*(e^* + p^*) \end{bmatrix}, \quad \vec{F}_{jv}^* = \begin{bmatrix} 0 \\ -\tau_{1j}^* \\ -\tau_{2j}^* \\ -\tau_{1j}^* u_1^* - \tau_{2j}^* u_2^* - k^* \frac{\partial T^*}{\partial x_j^*} \end{bmatrix} \tag{3}$$

with $j \in \{1, 2\}$. In Eq. (3), δ_{ij} $(i = 1, 2)$ is the Kronecker Delta function. In the perfect gas assumption, pressure and energy are given by

$$p^* = \rho^* R^* T^* \tag{4}$$

$$e^* = \rho^* c_v^* T^* + \frac{\rho^*}{2}(u_1^{*2} + u_2^{*2}) \tag{5}$$

where c_v^* is the specific heat at constant volume. For compressible Newtonian flow, the viscous stress tensor can be written as:

$$\tau_{ij}^* = \mu^* \left(\frac{\partial u_i^*}{\partial x_j^*} + \frac{\partial u_j^*}{\partial x_i^*} \right) - \frac{2}{3}\mu^* \left(\frac{\partial u_1^*}{\partial x_1^*} + \frac{\partial u_2^*}{\partial x_2^*} \right) \delta_{ij} \tag{6}$$

with $i, j \in \{1, 2\}$. In the simulation, the viscosity coefficient, μ^*, and the heat conductivity coefficient, k^*, are calculated using the Sutherland's law together with a constant Prandtl number, Pr. They are both functions of temperature only.

$$\mu^* = \mu_r^* \left(\frac{T^*}{T_r^*} \right)^{3/2} \frac{T_r^* + T_s^*}{T^* + T_s^*} \tag{7}$$

$$k^* = \frac{\mu^* c_p^*}{Pr} \tag{8}$$

where $\mu_r^* = 1.7894 \times 10^{-5}$ Ns/m^2, $T_r^* = 288.0$ K, $T_s^* = 110.33$ K, and c_p^* is the specific heat at constant pressure.

In this paper, the dimensional flow variables are non-dimensionalized by free-stream parameters. Specifically, density, temperature, velocity, and pressure are non-dimensionalized by ρ_∞^*, T_∞^*, u_∞^*, and $\rho_\infty^* u_\infty^{*2}$. Furthermore, x_1^* is non-dimensionalized by unit length in meter, whereas x_2^* is non-dimensionalized by the local boundary-layer thickness, $\sqrt{\mu_\infty^* x_1^* / \rho_\infty^* u_\infty^*}$. Referring to the coordinate system shown in Fig. 2, x_1^* and x_2^* are x^* and y^*, respectively. The two variables, u_1^* and u_2^*, are velocities in streamwise and wall-normal directions.

The fifth-order shock-fitting finite difference method of Zhong [18] is used to solve the governing equations in a domain bounded by the bow shock and the flat plate. In orther words, the bow shock is treated as a boundary of the computational domain. The Rankine-Hugoniot relation across the shock and a characteristic compatibility relation coming from downstream flow field are combined to solve the flow variables behind the shock. The shock-fitting method makes it possible for the Navier-Stokes equations to be spatially discretized by high-order finite difference methods. Specifically, a fifth-order upwind scheme is applied to discretize the inviscid flux derivatives. Meanwhile, a sixth-order central scheme is used for the discretization of viscous flux derivatives. By using the shock-fitting method, the interaction between the bow shock and wall forcing induced perturbations is solved as a part of solutions with the position and velocity of the shock front being taken as dependent flow variables. A three-stage semi-implicit Runge Kutta method of Zhong et al. [19] is used for temporal integration. In the leading edge region, there exists a singular point at the tip of the flat plate, which introduces numerical instability if the fifth-order shock-fitting method is used to simulate the flow. Therefore, the computational domain for the shock-fitting simulation starts from a very short distance downstream of the leading edge. A second-order TVD scheme used by Zhong and Lee [20] is applied to simulate the steady base flow in a small region including the leading edge to supply inlet conditions for the shock-fitting simulation. In receptivity simulations, two-dimensional wall perturbations are introduced in a downstream region where the shock-fitting method is used.

The same numerical method has been extensively used by our UCLA group in receptivity studies of supersonic and hypersonic boundary layers over a flat plate and a sharp wedge to various free-stream disturbances and surface roughness [9, 21, 22, 23]. The good agreement between numerical and LST results indicates that the fifth-order shock-fitting finite difference method is accurate to simulate the receptivity problems of high-speed boundary-layer flows. The numerical method has also been validated in the theoretical study and comparison with numerical simulation of Tumin, Wang, and Zhong [17]. The numerical perturbation field downstream of the blowing-suction actuator is decomposed into boundary-layer wave modes with the help of the biorthogonal eigenfunction system. The filtered-out amplitudes of mode S and mode F agree well with the corresponding theoretical solutions of linear receptivity problem.

3 Flow Conditions and Models of Porous Coating

Free-stream flow conditions of the currently studied flow are the same as those of Maslov et al.'s experiment [4], i.e.,

$$\begin{array}{ll} M_\infty = 5.92\,, & T^*_\infty = 48.69\mathrm{K}\,, \\ p^*_\infty = 742.76\mathrm{Pa}\,, & Pr = 0.72\,, \\ f^* = 50\mathrm{kHz}\,, & \mathrm{F} = 26.51\times 10^{-6}\,, \\ Re^*_\infty = 13\times 10^6/\mathrm{m} & \end{array}$$

where Re^*_∞ is the unit Reynolds number defined as

$$Re^*_\infty = \rho^*_\infty u^*_\infty / \mu^*_\infty \tag{9}$$

The dimensional streamwise coordinate, x^* as shown in Fig. 2, can be converted to local Reynolds number by

$$Re_x = Re^*_\infty \; x^* \tag{10}$$

In LST studies of boundary-layer flows, the Reynolds number based on the local length scale of boundary-layer thickness, L^*, is generally used. They are expressed as

$$R = \frac{\rho^*_\infty u^*_\infty L^*}{\mu^*_\infty}, \quad L^* = \sqrt{\frac{\mu^*_\infty x^*}{\rho^*_\infty u^*_\infty}} \tag{11}$$

Hence, the relation between R and local Reynolds number Re_x is given by

$$R = \sqrt{Re_x} \tag{12}$$

For the simulation of mean flow, the wall is adiabatic, and the physical boundary condition of velocity on the flat plate is the non-slip condition. When porous coating is used, the isothermal temperature condition is applied on porous region. This temperature condition is a standard boundary condition for theoretical and numerical studies of high frequency disturbances. Meanwhile, non-slip condition is applied on the wall except the porous region. Inlet conditions are specified, while high-order extrapolation is used for outlet conditions because the flow is hypersonic at the exit boundary except a small region near the flat plate. The flow variables behind the shock are solved by combining Rankine-Hugoniot relation across the shock and a characteristic compatibility relation coming from downstream flow field.

In current study, stability simulations based on mean flow consist of three steps: 1. disturbances corresponding to a specific boundary-layer wave (mode S or mode F) at a frequency of 100 kHz are introduced at the inlet of the computational domain to study its spatial development; 2. porous coating is used to investigate its effect on the spatial development of mode S and mode F; 3. multiple porous coatings are used to study the effect of porous coating location on the spatial development of mode S and mode F.

At step 1, disturbances corresponding to a specific boundary-layer wave at a frequency of 100 kHz are introduced at the inlet of the computational domain. The disturbances are a combination of velocity, pressure, and temperature oscillations, which can be expressed as,

$$\left\{ \begin{array}{c} \tilde{u^*} \\ \tilde{v^*} \\ \tilde{w^*} \\ \tilde{p^*} \\ \tilde{T^*} \end{array} \right\} = \epsilon \left\{ \begin{array}{c} \hat{u^*}(y^*) \\ \hat{v^*}(y^*) \\ \hat{w^*}(y^*) \\ \hat{p^*}(y^*) \\ \hat{T^*}(y^*) \end{array} \right\} \sin(\omega^* t^*) \tag{13}$$

where ϵ is a small dimensionless parameter representing the amplitude of disturbances. The vector, $\{\hat{u^*}(y^*),\ \hat{v^*}(y^*),\ \hat{w^*}(y^*),\ \hat{p^*}(y^*),\ \hat{T^*}(y^*)\ \}^{\mathrm{T}}$, represents the eigenfunction of the specific boundary-layer wave, which is normalized by the pressure perturbation on the wall. In above equation, ω^* is the circular frequency of the disturbances, which is related to the frequency by

$$\omega^* = 2\pi f^* \tag{14}$$

The circular frequency, ω^*, and the frequency, f^*, are non-dimensionalized according to

$$\omega = \frac{\omega^* L^*}{u^*_\infty} \tag{15}$$

$$F = \frac{2\pi f^* \mu^*_\infty}{\rho^*_\infty u^{*2}_\infty} = \frac{\omega^* \mu^*_\infty}{\rho^*_\infty u^{*2}_\infty} \tag{16}$$

With the definitions of Reynolds number R and the dimensionless frequency F, the dimensionless circular frequency can also be expressed as

$$\omega = RF \tag{17}$$

The model of the coating is the same as that of Fedorov et al. [1], i.e., blowing-suction relating to the local pressure oscillation.

$$v\prime = A_y p\prime \tag{18}$$

The porous coating admittance, A_y, is defined as

$$A_y = -\frac{\phi}{Z_0}\tanh(\Lambda h) \tag{19}$$

In above equation, ϕ is porosity, h is the porous-layer thickness non-dimensionalized by the local length scale of boundary layer thickness.

$$h = \frac{h^*}{L^*} = \frac{h^*}{\sqrt{\frac{\mu^*_\infty x^*}{\rho^*_\infty u^*_\infty}}} \tag{20}$$

Based on Allard and Champoux's theoretical analysis [24], the empirical equations for porous coating characteristic impedance (Z_0) and propagation constant (Λ) are

$$Z_0 = \frac{\rho_w}{M_e}\sqrt{\frac{T_w \tilde{\rho}}{\tilde{C}}} \tag{21}$$

$$\Lambda = \frac{i\omega M_e}{\sqrt{T_w}}\sqrt{\tilde{\rho}\tilde{C}} \tag{22}$$

where ρ_w and T_w are the local dimensionless density and temperature on coating. The edge Mach number (M_e) is defined right after the shock wave. The dynamic density ($\tilde{\rho}$) and bulk modulus ($\tilde{C}$) are calculated using the following two equations.

$$\tilde{\rho} = a_\infty[1 + \frac{g(\lambda_1)}{\lambda_1}] \tag{23}$$

$$\tilde{C} = \gamma - \frac{\gamma - 1}{1 + \frac{g(\lambda_2)}{\lambda_2}} \tag{24}$$

where λ_1, λ_2, and the function $g(\lambda)$ are defined as

$$g(\lambda) = \sqrt{1 + \frac{4a_\infty \mu_w^* \lambda}{\sigma^* \phi r_p^{*2}}} \tag{25}$$

$$\lambda_1 = \frac{i a_\infty \rho_w^* \omega^*}{\phi \sigma^*} \tag{26}$$

$$\lambda_2 = 4\mathrm{Pr}\lambda_1 \tag{27}$$

where a_∞ is the tortuosity, σ^* is the flow resistivity, and r_p^* is the characteristic pore size. These parameters are determined by the porous coating. In porous coating model, the local dimensionless variables (v, p, T_w, ρ_w, ω) are non-dimensionalized by the corresponding variables right after the shock wave (u_e^*, $\rho_e^* u_e^{*2}$, T_e^*, ρ_e^*, $\sqrt{\mu_e^* x^* / \rho_e^* u_e^*}/u_e^*$).

According to the definitions of characteristic impedance and propagation constant, the porous coating admittance is generally a complex number. And the pressure perturbation is also a complex number. However, only the real part of velocity perturbation can be imposed on the coating in numerical simulations. In this way, the velocity perturbation is written relating to the real part of pressure perturbation ($p(t^*)$) as

$$v(t^*) = \mathrm{Real}(A_y)p(t^*) - \mathrm{Imag}(A_y)p(t^* - \frac{\pi}{2\omega^*}) \tag{28}$$

where "Real(A_y)" and "Imag(A_y)" represent the real part and imaginary part of porous coating admittance, respectively.

4 Results and Discussions

4.1 Steady base flow

The steady base flow over the flat plate is simulated by solving the two-dimensional compressible Navier-Stokes equations with a combination of a fifth-order shock-fitting finite difference method and a second-order TVD scheme. In the leading edge region, there exists a singular point at the tip of the flat plate, which will introduce numerical instability if the fifth-order shock-fitting method is used to simulate the flow. Therefore, a second-order TVD scheme used by Zhong and Lee [20] is applied to simulate the steady base flow in a small region including the leading edge. The computational domain for the fifth-order shock-fitting method starts at $x^* = 0.0025$ m and ends at $x^* = 0.879$ m, corresponding to $R = 180.28$ and $R = 3380.38$, respectively. In actual shock-fitting simulations, the computational domain is divided into 19 zones with a total of 3746 grid points in streamwise direction. The number of grid points in wall-normal direction is 121 upstream of the position of $x^* = 0.309$ m and 176 downstream of that position. Forty-one points are used in the overlapped region between two neighboring zones, which is proved to be sufficient to make the solution accurate and smooth within the whole domain. An exponential stretching function is used in the wall-normal direction to cluster more points inside the boundary layer. On the other hand, the grid points are uniformly distributed in streamwise direction. The spatial convergence of the results based on this grid structure has been evaluated by grid refinement studies to ensure the grid independence of the fifth-order shock-fitting simulations.

For shock-fitting simulation in the first zone, the inlet conditions are obtained from the results of the second-order TVD shock-capturing scheme which is used to simulate the steady base flow in a small region including the leading edge. For shock-fitting simulations in other zones, inlet conditions are interpolated from the results of the previous zone. The computational domain for the second-order TVD scheme starts at $x^* = -0.0005$ m and ends at $x^* = 0.0035$ m. Three sets of grid structures are used to check the grid independence of the numerical results. Figure 3 compares the density contours near the leading edge simulated by second-order TVD scheme based on three sets of grid structures. It shows that the contours on 201×176 mesh agree well with those on 241×181 mesh whereas they have significant discrepancies with the contours on 161×101 mesh. This figure indicates that the grid structure of 201×176 is fine enough to ensure the grid independence of numerical results. However, the grid structure of 161×101 is too coarse to achieve spatially converged numerical results. Similar conclusion can be drawn in Fig. 4, where the density distributions in wall-normal direction are compared. In this figure, the density distributions are evaluated at $x^* = 0.0025$ m, the initial location of the first zone.

In order to validate the combination of fifth-order shock-fitting method and second-order TVD scheme, Figs. 5 and 6 plot density and wall-normal velocity contours near the leading edge of the steady base flow obtained by the combination of second-order TVD scheme and fifth-order shock-fitting method. The flow field including the leading edge is simulated by the TVD scheme, while the flow field after $x^* = 0.0025$ m is simulated by the shock-fitting method. These figures show that density and wall-normal velocity contours calculated by the two methods have a good agreement near the upstream edge of the overlapped region, which indicates that the TVD solutions are accurate enough to be used as inlet conditions for the fifth-order shock-fitting simulation in the first zone. The small discrepancies of the contours near the bow shock are caused by viscous effect. Due to viscosity, the bow shock has a finite thickness for TVD simulation, while it is assumed to be infinitely thin for the shock-fitting simulation. The combination of fifth-order shock-fitting method and second-order TVD scheme has also been validated in cases of supersonic and hypersonic steady base flows by Ma & Zhong [25] and Wang & Zhong [2].

To validate the accuracy of numerical simulation, the steady base flow simulated by the fifth-order shock-fitting method is compared with Maslov et al.'s experimental measurements and the theoretical self-similar boundary-layer solution. According to Maslov et al.'s experiments, effect of the viscous-inviscid interaction is strong within the region of 0.2 mm $< x^* <$ 33 mm. Figures 7 shows that pressure has large gradients upstream of the location of $x^* = 33$ mm, which is consistent with the experimental results. Figure 8 shows the distributions of dimensionless streamwise velocity across the boundary layer at three different locations. It shows that the thickness of the boundary layer increases with the location shifting downstream. At $x^* = 96$ mm, 121 mm, and 138 mm, the thicknesses of the boundary layer are approximately equal to 1.84 mm, 2.04 mm, and 2.20 mm, which has a good agreement with Maslov et al.'s experimental measurements of about 1.8 mm, 2.0 mm, and 2.2 mm, respectively.

Figures 9 and 10 compare normalized Mach number M/M_∞ and dimensionless streamwise velocity u^*/u^*_∞ distributions across the boundary layer at three different locations of $x^* = 96$ mm, 121 mm, and 138 mm. In these figures, η is defined as $\eta = y^*/L^*$. The solid lines represent distributions of M/M_∞ and u^*/u^*_∞ obtained by solving the compressible boundary-layer equations. Due to the fact that the theoretical solution of boundary-layer equations is self-similar, the distributions of M/M_∞ and u^*/u^*_∞ at different locations are exactly the same. The unfilled symbols represent experimental results of Maslov et al., whereas the other three lines stand for numerical simulation results. The good agreement between the simulation results indicate that an approximate gradientless flow is obtained over the flat plate, which is evaluated in Maslov et al.'s paper by comparing the experimental results. The approximate gradientless flow is clearly shown in Fig. 7. Figures 9 and 10 show that the numerical results agree well with the experimental results and the boundary-layer solution near the plate. However, in the region of $\eta > 5$, the numerical results have a better agreement with the experimental results. The difference between the numerical results and the boundary-layer solution is mainly caused by viscous-inviscid interaction, because the effect of the bow shock is neglected in the calculation of the compressible boundary-layer equations. The analysis of Figs. 8, 9, and 10 indicate that the hypersonic steady base flow considered in the current study is accurately simulated by the fifth-order shock-fitting method.

4.2 Stability characteristics of boundary-layer wave modes

The stability characteristics of boundary-layer wave modes of the Mach 5.92 flow is studied by LST based on a multi-domain spectral method of Malik [26]. The velocity, pressure, and temperature disturbances are represented by harmonic waves of the form

$$\left\{\begin{array}{c}\tilde{u}\\ \tilde{v}\\ \tilde{w}\\ \tilde{p}\\ \tilde{T}\end{array}\right\} = \left\{\begin{array}{c}\hat{u}(y)\\ \hat{v}(y)\\ \hat{w}(y)\\ \hat{p}(y)\\ \hat{T}(y)\end{array}\right\} e^{i(\alpha_c x+\beta_c z-\omega_c t)} \tag{29}$$

The parameters of α_c and β_c are wave number components in streamwise and spanwise directions, and ω_c is the circular frequency. For two-dimensional wall perturbations, $\beta_c = 0$. Substituting disturbances of Eq. (29) and the steady base flow into the compressible linearized Navier-Stokes equations, an ordinary-differential-equation system is achieved, i.e.,

$$(A\frac{d^2}{dy^2} + B\frac{d}{dy} + C)\phi = 0 \tag{30}$$

where ϕ is the disturbance vector defined by $\{\hat{u}, \hat{v}, \hat{p}, \hat{T}, \hat{w}\}^{\mathrm{T}}$. The coefficient matrices of A, B, and C are given in Malik's paper [26]. In spatial stability analysis, the two parameters, ω_c and β_c, are specified as real numbers. The streamwise wave number, α_c, is a complex number and solved as the eigenvalue of the ordinary-differential-equation system. The complex wave number α_c can be expressed as

$$\alpha_c = \alpha_r + i\alpha_i \tag{31}$$

where α_i is the local growth rate. A boundary-layer wave mode is unstable when $\alpha_i < 0$ whereas it is stable when $\alpha_i > 0$. The points $\alpha_i = 0$ are called the neutral points of the boundary-layer wave mode. A wave mode is generally unstable only in certain domains bounded by the neutral points. The real part, α_r, is the local wave number which can be used to define the local phase velocity:

$$a = \frac{\omega_c}{\alpha_r} \tag{32}$$

Both the wave number and the phase velocity can be used to identify the boundary-layer wave mode.

Figure 11 shows eigenvalue spectra of wave number α of the boundary-layer wave modes for a case with a frequency of $f^* = 100$ kHz at $x^* = 0.189$ m ($F = 53.03 \times 10^{-6}$, $R = 1567.48$). The figure shows the wave spectra corresponding to fast acoustic mode, entropy and vorticity mode, and slow acoustic mode. The two discrete modes marked by circles are mode F and mode S, which is validated by the corresponding eigenfunctions of u'_r and p'_r as shown in Figs. 12 and 13. The two figures show that the eigenfunctions are approximately equal to zero out of the boundary layer, which indicates that the two discrete modes exist in the boundary layer. Mode F is a stable mode, which was called Mode I by Ma and Zhong [21, 22]. This mode originates from the fast acoustic spectrum on the left side of the figure and passes the entropy and vorticity spectra at the center as dimensionless frequency increases. Mode S originates from the slow acoustic spectrum on the right side of the figure. It becomes unstable in certain range of dimensionless frequency. The figure also shows that mode S at the frequency of $f^* = 100$ kHz is unstable at $x^* = 0.189$ m with $\alpha_i < 0$.

Figure 14 shows the dimensionless phase velocities of boundary-layer wave modes at two locations of $x^* = 0.159$ m and $x^* = 0.189$ m as a function of the dimensionless circular frequency. The three horizontal dashed lines represent the dimensionless phase velocities of fast acoustic mode ($a = 1 + M_\infty^{-1}$), entropy and vorticity modes ($a = 1$), and slow acoustic mode ($a = 1 - M_\infty^{-1}$), respectively. The excellent agreement of the phase velocities at different locations indicates that the phase velocity is approximately a function of dimensionless circular frequency only. The figure clearly shows that mode F originates from fast acoustic mode. As ω increases, the phase velocity of mode F decreases. When mode F passes the continuous entropy and vorticity modes near $\omega = 0.1$, there exists a jump of phase velocity, which is consistent with the theoretical analysis of Fedorov and Khokhlov [27]. On the other hand, mode S originates from slow acoustic mode. The figure also shows that mode S synchronizes with mode F at the point of $\omega_s = 0.11563$ and $a_s = 0.93076$.

Although Fig. 14 shows that the synchronization point has a constant value of dimensionless circular frequency ($\omega_s = 0.11563$), the dimensional location of the synchronization point, x^*_{sn}, are different for different dimensionless frequencies. The synchronization location in x^* coordinate for a given dimensionless frequency can be calculated using the following formula

$$x^*_s = \frac{(\omega_s/F)^2}{Re^*_\infty} \tag{33}$$

This equation indicates that the synchronization point moves upstream with the dimensionless frequency increasing.

Figure 15 shows the growth rates of mode S and mode F at the same set of locations as a function of the dimensionless circular frequency ω. The horizontal dotted line stands for the neutral modes ($\alpha_i = 0$). In Fig. 15, the growth rates of mode S of the two locations agree well, and they are approximately functions of ω only. Mode S is unstable in the region from $\omega_I = 0.00827$ to $\omega_{II} = 0.18465$. For unstable mode S, it is also noticed that the growth rate upstream of $\omega = 0.095$ is much larger than those around and downstream of it. This indicates that mode S is more unstable around and downstream of $\omega = 0.095$. The parameters ω_I and ω_{II} are called the Branch I and Branch II neutral points of mode S. The figure shows that mode S is stable upstream of Branch I neutral point and downstream of Branch II neutral point. The locations of the Branch I and Branch II neutral points in x^* coordinate, which changes with different dimensionless frequencies, can be calculated by

$$x^*_I = \frac{(\omega_I/F)^2}{Re^*_\infty} \tag{34}$$

$$x_{II}^* = \frac{(\omega_{II}/F)^2}{Re_\infty^*} \tag{35}$$

Equations (34) and (35) shows that when F increases, the corresponding x_I^* and x_{II}^* decrease. In other words, the Branch I and Branch II neutral point move upstream when F increases.

4.3 Effect of porous coating on mode S

In current study, parameters of porous coating are the same as those used in Fedorov et al.'s paper [1], i.e.,

$$\begin{array}{ll} \phi = 0.75\,, & h^* = 0.75\text{mm}\,, \\ a_\infty = 1\,, & d^* = 30\mu\text{m}\,, \\ \sigma^* = 1.66 \times 10^5 \text{kg}(\text{m}^3\text{s}^{-1})\,, & \gamma = 1.4 \end{array}$$

where d^* is the fiber diameter, which is related to the characteristic pore size as follows:

$$r_p^* = \frac{\pi d^*}{2 - 3\phi + \phi^2} \tag{36}$$

As has been mentioned, stability simulations consist of three steps: 1. disturbances corresponding to a specific boundary-layer wave (mode S or mode F) at a frequency of 100 kHz are introduced at the inlet of the computational domain to study its spatial development; 2. porous coating is used to investigate its effect on the spatial development of mode S and mode F; 3. multiple porous coatings are used to study the effect of porous coating location on the spatial development of mode S and mode F. Specifically, four cases of stability simulations are considered to investigate the effect of porous coating and its location on boundary-layer waves,

- Case 1: no porous coating;
- Case 2: one porous coating;
- Case 3: two porous coatings, where the first one is the same as that in Case 2;
- Case 4: three porous coatings, where the first two are the same as those in Case 3;

For all cases considered in current paper, porous coatings are located upstream of the corresponding synchronization point of mode S and mode F at $x_s^* = 0.33184$ m. Numerical simulations on cases with porous coating located downstream of the synchronization point will be carried out as the next step. The locations of porous coating for the four cases are schematically shown in Fig. 16. Quantitativly, the three porous coatings are located on the wall in three regions: $(73.65, 124.65)$ mm, $(193.65, 244.65)$ mm, $(283.65, 304.65)$ mm. The computational domain for stability simulation starts at $x^* = 69.00$ mm and ends at $x^* = 0.8590$ m.

In this section, disturbances corresponding to mode S at a frequency of 100 kHz are introduced at the inlet of the computational domain ($x^* = 69.00$ mm). The parameter of disturbance amplitude, ϵ in Eq. (13), is assigned as

$$\epsilon = 1.0 \times 10^{-8} \tag{37}$$

This parameter is small enough to preserve the linear properties of the disturbances. Figure 17 compares disturbance profiles introduced at the inlet with the eigenfunction of mode S obtained from LST. In the figure, both numerical disturbances and eigenfunction of mode S are normalized by corresponding pressure perturbation on the wall. The good agreements of velocity and pressure profiles indicate that the disturbances introduced at the inlet is exactly mode S. The discrepancy between temperature profiles near the wall ($y/L < 15$) as shown in Fig. 17(d) is caused by nonparallel flow effect, because temperature profile of numerical disturbance is calculated from the eigenfunction of mode S with the help of mean flow temperature, pressure, and density, i.e.,

$$\tilde{T^*} = T_0^*\left(\frac{\tilde{p^*}}{p_0^*} - \frac{\tilde{\rho^*}}{\rho_0^*}\right) \tag{38}$$

where T_0^*, p_0^*, and ρ_0^* are mean flow temperature, pressure, and density. $\tilde{p^*}$ and $\tilde{p^*}$ are pressure and density components of mode S eigenfunction.

Figures 18 shows amplitude distributions of pressure perturbation along the flat plate for the four cases of stability simulations. It is noticed that porous coating increases pressure perturbation amplitude downstream of the porous region. With the number of porous coatings increasing, pressure perturbation amplitude keeps increasing. However, the effect of porous coating on mode S in porous region is not consistent. With the location of porous coating shifting from upstream to downstream, the effect of porous coating on mode S changes from destabilization to stabilization. To show clearly the spatial development of mode S in porous region, Figure 19 compares pressure perturbation amplitude obtained from numerical simulation with porous coating with that obtained from numerical simulation without porous coating. This figure shows that the effect of porous coating on mode S in porous region strongly depends on the location of porous coating. For porous coating located in the region $(73.65, 124.65)$ mm, pressure perturbation amplitude decreases initially then quickly increases. For porous coating located in the region $(193.65, 244.65)$ mm, pressure perturbation amplitude increases in the whole region. For porous coating located in the region $(283.65, 304.65)$ mm, pressure perturbation amplitude decreases in the whole region.

Figures 20, 21, and 22 compare normalized pressure perturbation amplitudes obtained from numerical simulations with/without porous coating at six locations in three regions of $(73.65, 124.65)$ mm, $(193.65, 244.65)$ mm, $(283.65, 304.65)$ mm, respectively. All these three figures show that the profiles of pressure perturbation at the leading and trailing edges of porous coating change significantly due to the singularity of wall blowing-suction at the edges of porous region. However, pressure perturbation in porous region keeps similar profile as mode S, which indicates that porous coating does't change mode S to other mode but stabilizes or destabilizes mode S. From upstream to downstream, Figures (b) to (e) show the propagation of mach waves induced by the leading edge of porous coating from wall to outside of the boundary layer.

In order to investigate the spatial development of mode S quantitatively, a local wave number (α_r) and a local growth rate (α_i) related to pressure perturbation along the flat plate are calculated by

$$\alpha_r = L^* \frac{d\phi'}{dx^*} \tag{39}$$

$$\alpha_n = -\frac{L^*}{|p'|} \frac{d|p'|}{dx^*} \tag{40}$$

where L^* is the length scale of local boundary layer thickness as defined by Eq. (11). $|p'|$ and ϕ' are pressure perturbation amplitude and phase angle, respectively. The parameters α_r and α_i will represent the true wave number and growth rate only if the perturbation is dominated by a single wave mode. Otherwise, the disturbance needs to be decomposed in odrer to check properties of a specific mode. For example, Tumin, Wang, and Zhong [17] decomposed the disturbance at a location just downstream of the blowing-suction actuator with a biorthogonal eigenfunction system, where mode F, mode S, and acoustic modes coexisted and none of them was dominant.

Since our focus is on numerical simulation results, we only consider the later stage where mode S is the dominant mode in the boundary layer. In this case, Eqs. (39) and (40) can be used to check the properties of the unstable mode S. Figure 23 compares the growth rate calculated from numerical simulation results with that obtained from LST for the four cases of stability simulations. The growth rate of numerical simulation results has a good agreement with that of LST in the region from $\omega = 0.11$ to $\omega = 0.13$. When ω is larger than 0.13, the growth rate of numerical simulation results are larger than that of LST, i.e., mode S obtained by numerical simulation becomes more stable than that predicted by LST. Figure 24 compares the phase velocity (ω/α_r) calculated from numerical simulation results with that obtained from LST for the four cases of stability simulations. The agreement of the two sets of phase velocities in downstream region of $x^* > 0.30$ m confirms that mode S is the dominant mode in the boundary layer. The agreement in phase velocity is not so good in early region where porous coating are used.

4.4 Effect of porous coating on mode F

In this section, disturbances corresponding to mode F at a frequency of 100 kHz are introduced at the inlet of the computational domain. Similarly, four cases of stability simulations are considered to investigate the effect of porous coating and its location on the spatial development of mode F. The locations of porous coating for the four cases are schematically shown in Fig. 16. Quantitativly, the three porous coatings are located on the wall in three regions: (73.65, 124.65) mm, (193.65, 244.65) mm, (283.65, 304.65) mm. The computational domain for stability simulation starts at $x^* = 69.00$ mm and ends at $x^* = 0.8590$ m. The parameter of disturbance amplitude, ϵ in Eq.

(13), is assigned as

$$\epsilon = 1.0 \times 10^{-6} \tag{41}$$

Although the amplitude of disturbance corresponding to mode F at the inlet is one hundred times of corresponding to mode S, this parameter is still small enough to preserve the linear properties of the disturbances, because mode F is stable.

Figure 25 compares numerical disturbance profiles introduced at the inlet with the eigenfunction of mode F obtained from LST. In the figure, both numerical disturbances and eigenfunction of mode F are normalized by corresponding pressure perturbation on the wall. The good agreements of velocity and pressure profiles indicate that the disturbances introduced at the inlet is exactly mode F. Similarly, the discrepancy between temperature profiles near the wall ($y/L < 15$) as shown in Fig. 25(d) is caused by nonparallel flow effect.

Figures 26 shows amplitude distributions of pressure perturbation along the flat plate for the four cases of stability simulation. It is also noticed that porous coating increases pressure perturbation amplitude downstream of the porous region. With the number of porous coatings increasing, pressure perturbation amplitude keeps increasing. Generally, porous coating decreases pressure perturbation in porous region, i.e., porous coating stabilizes mode F in porous region. To show clearly the spatial development of mode F in porous region, Figure 27 compares pressure perturbation amplitude obtained from numerical simulation with porous coating with that obtained from numerical simulation without porous coating. This figure shows that the effect of porous coating on mode S in porous region also depends on the location of porous coating. For porous coating located in the region $(73.65, 124.65)$ mm, pressure perturbation amplitude decreases in the whole region. Similar phenomenon is observed for porous coating located in the region $(283.65, 304.65)$ mm. However for porous coating located in the region $(193.65, 244.65)$ mm, pressure perturbation amplitude decreases initially then increases near the trailing edge of the porous region.

Figures 28, 29, and 30 compare normalized pressure perturbation amplitudes obtained from numerical simulations with/without porous coating at six locations in three regions of $(73.65, 124.65)$ mm, $(193.65, 244.65)$ mm, $(283.65, 304.65)$ mm, respectively. All these three figures show that the profiles of pressure perturbation at the leading and trailing edges of porous coating change significantly due to the singularity of wall blowing-suction at the edges of porous region. From upstream to downstream, Figures (b) to (e) show the propagation of mach waves induced by the leading edge of porous coating from wall to outside of the boundary layer. Compared with Figs. 20, 21, and 22, these three figures also show that porous coating excites much stronger mach waves when the disturbances introduced at the inlet is mode F. Figures 28 and 29(b) to (d) show that pressure perturbation in porous region keeps similar profile as mode F, which indicates that porous coating does't change mode F to other mode but stabilizes mode F. Figures 29(e) and 30 show that pressure perturbation in porous region is similar to the profile of mode S, which indicates that mode F changes to mode S in this region. As a result, the effects of porous coating on mode S and mode F in the region $(283.65, 304.65)$ mm are quite similar, as shown in Figs. 19 and 27.

Figure 31 compares the growth rate calculated from numerical simulation results with that obtained from LST for the four cases of stability simulations. All cases show that mode F changes to mode S near the synchronization point. After the change, the growth rate of numerical simulation results has a good agreement with that of LST in the region from $\omega = 0.11$ to $\omega = 0.13$. When ω is larger than 0.13, the growth rate of numerical simulation results are larger than that of LST, i.e., mode S obtained by numerical simulation becomes more stable than that predicted by LST. Figure 32 compares the phase velocity (ω/α_r) calculated from numerical simulation results with that obtained from LST for the four cases of stability simulations. It is clearly shown that mode F changes to mode S around $x^* = 0.32$ m. The agreement of the two sets of phase velocities in downstream region of $x^* > 0.30$ m confirms that mode S is the dominant mode in the boundary layer.

5 Summary

The effect of porous coating and its location on the spatial developments of mode S and mode F in a Mach 5.92 flat-plate boundary layer is investigated by linear stability theory (LST) and direct numerical simulation (DNS). The mean flow is calculated by solving compressible Navier-Stokes equations with a combination of a fifth-order shock-fitting method and a second-order total variation diminishing (TVD) scheme. The stability characteristics of the hypersonic boundary layer is analyzed by LST. Stability simulations based on mean flow consist of three steps: 1. disturbances corresponding to a specific boundary layer wave (mode S or mode F) at a frequency of 100 kHz are introduced at the inlet of the computational domain to study its spatial development; 2. porous coating is used to investigate its effect on the spatial development of mode S and mode F; 3. multiple porous coatings are used to study the effect of porous coating location on the spatial development of mode S and mode F. The same theoretical model of porous coating as that in Fedorov et al.'s paper is used, i.e., porous coating is modelled by pressure perturbation related wall blowing-suction. For all the cases considered in current paper, porous coatings are located upstream of the corresponding synchronization point of mode S and mode F at $x_s^* = 0.33184$ m. The numerical results show that porous coating and its location have significant effects on the spatial developments of mode S and mode F. No matter which mode of mode S and mode F is introduced at the inlet, porous coating increases pressure perturbation amplitude downstream of the porous region. With the number of porous coatings increasing, pressure perturbation amplitude keeps increasing. In case of mode S, the effect of porous coating on mode S in porous region is not consistent. With the location of porous coating shifting from upstream to downstream, the effect of porous coating on mode S changes from destabilization to stabilization. In case of mode F, all cases show that mode F changes to mode S near the synchronization point and mode F is stabilized in porous region.

Acknowledgments

This work was sponsored by the Air Force Office of Scientific Research, USAF, under AFOSR Grant #FA9550-04-1-0029 and #FA9550-07-1-0414, monitored by Dr. John Schmisseur. The views and conclusions contained herein are those of the authors and should not be interpreted as necessarily representing the official policies or endorsements either expressed or implied, of the Air Force Office of Scientific Research or the U.S. Government.

References

[1] A. Fedorov, A. Shiplyuk, A. Maslov, E. Burov, and N. Malmuth. Stabilization of a hypersonic boundary layer using an ultrasonically absorptive coating. *Journal of Fluid Mechanics*, Vol. 479, pp. 99-124, 2003.

[2] X. Wang and X. Zhong. Receptivity of A Mach 8.0 Flow over A Sharp Wedge to Wall Blowing-Suction. *AIAA paper 2005-5025*, June 2005.

[3] X. Wang and X. Zhong. Role of the synchronization point on boundary layer stabilization using porous coating. *AIAA paper 2008-4382*, June 2008.

[4] A. A. Maslov, A. N. Shiplyuk, A. Sidorenko, and D. Arnal. Leading-edge receptivity of a hypersonic boundary layer on a flat plate. *Jounral of Fluid Mechanics*, Vol.426, pp.73-94, 2001.

[5] L. Lees and C. C. Lin. Investigation of the stability of the laminar boundary layer in compressible fluid. *NACA TN No. 1115*, 1946.

[6] L. M. Mack. Linear Stability Theory and the Problem of Supersonic Boundary-Layer Transition. *AIAA Journal*, Vol.13, No.3, pp.278-289, 1975.

[7] J. M. Kendall. Wind Tunnel Experiments Relating to Supersonic and Hypersonic Boundary-Layer Transition. *AIAA Journal*, Vol.13, No.3, pp.290–299, 1975.

[8] M. R. Malik, R. S. Lin, and R. Sengupta. Computation of Hypersonic Boundary-Layer Response to External Disturbances. *AIAA Paper 1999-0411*, January 1999.

[9] Y. Ma and X. Zhong. Receptivity of a supersonic boundary layer over a flat plate. Part 3. Effects of different types of free-stream disturbances. *Journal of Fluid Mechanics*, Vol.532, pp.63-109, 2005.

[10] M. V. Morkovin, E. Reshotko, and T. Herbert. Transition in open flow systems - a reassessment. *Bulletin of the American Physical Society*, Vol. 39, pp. 1882, 1994.

[11] E. Reshotko. Is Re_θ/Me a meaningful transition criterion ? *AIAA paper 2007-0943*, January 2007.

[12] L. M. Mack. Boundary layer linear stability theory. In *AGARD report, No. 709*, pages 3–1 to 3–81, 1984.

[13] W. S. Saric. Laminar-turbulent transition: fundamentals. *AGARD R-786*, 1992.

[14] A. S. W. Thomas. The control of boundary-layer transition using a wave-superposition principle. *Journal of Fluid Mechanics*, Vol. 137, pp. 233-250, 1983.

[15] D. Sturzebecher and E. Nitsche. Active control of boundary-layer instabilities on an unswept wing. *Notes on Numerical Fluid Mechanics and Multidisciplinary Design*, Vol. 86, pp. 189-202, 2003.

[16] L. Yong and M. Gaster. Active control of boundary-layer instabilities. *Journal of Fluid Mechanics*, Vol. 550, pp. 185-205, 2006.

[17] A. Tumin, X. Wang, and X. Zhong. Direct numerical simulation and the theory of receptivity in a hypersonic boundary layer. *Physics of Fluids*, Vol. 19, Paper No. 014101, 2007.

[18] X. Zhong. High-Order Finite-Difference Schemes for Numerical Simulation of Hypersonic Boundary-Layer Transition. *Journal of Computational Physics*, Vol.144, pp. 662-709, 1998.

[19] X. Zhong. Additive Semi-Implicit Runge-Kutta Schemes for Computing High-Speed Nonequilibrium Reactive Flows. *Journal of Computational Physics*, Vol.128, pp.19-31, 1996.

[20] X. Zhong and T. Lee. Nonequilibrium real-gas effects on disturbance/bow shock interaction in hypersonic flow past a cylinder. *AIAA paper 1996-1856*, January 1996.

[21] Y. Ma and X. Zhong. Receptivity of a supersonic boundary layer over a flat plate. Part 1:Wave Structures and Interactions. *Journal of Fluid Mechanics*, Vol.488, pp.31-78, 2003.

[22] Y. Ma and X. Zhong. Receptivity of a supersonic boundary layer over a flat plate. Part 2:Receptivity to Freestream Sound. *Journal of Fluid Mechanics*, Vol.488, pp.79-121, 2003.

[23] X. Wang and X. Zhong. Receptivity of a hypersonic flat-plate boundary layer to three-dimensional surface roughness. *Journal of Spacecraft and Reckets*, Vol. 45, No. 6, pp. 1165-1174, 2008.

[24] J-F. Allard and Y. Champoux. New empirical equations for sound propagation in rigid frame fibrous materials. *The Journal of the Acoustical Society of America*, Vol. 91, No. 6, pp. 3346-3353, 1992.

[25] Y. Ma and X. Zhong. Receptivity to Freestream Disturbances of Mach 4.5 Flow over A Flat Plate. *AIAA Paper 2002-0140*, January 2002.

[26] M. R. Malik. Numerical methods for hypersonic boundary layer stability. *Journal of Computational Physics*, Vol.86, pp.376-413, 1990.

[27] A. V. Fedorov and A. P. Khokhlov. Prehistory of Instability in a Hypersonic Boundary Layer. *Theoretical and Computational Fluid Dynamics*, Vol. 14, pp. 359-375, 2001.

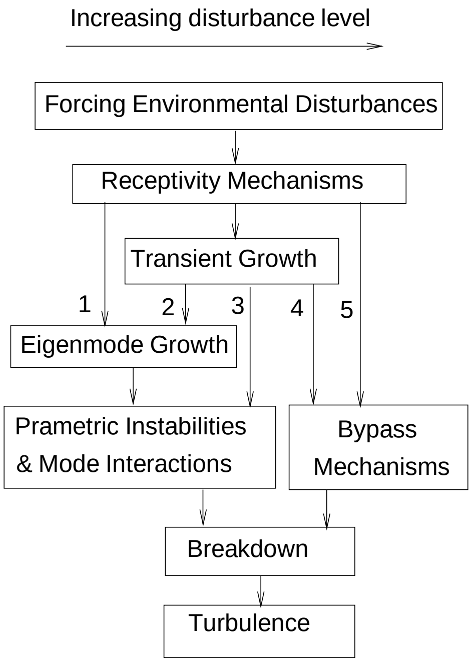

Figure 1: Paths of the transition process in boundary layers respecting to disturbance amplitude level.

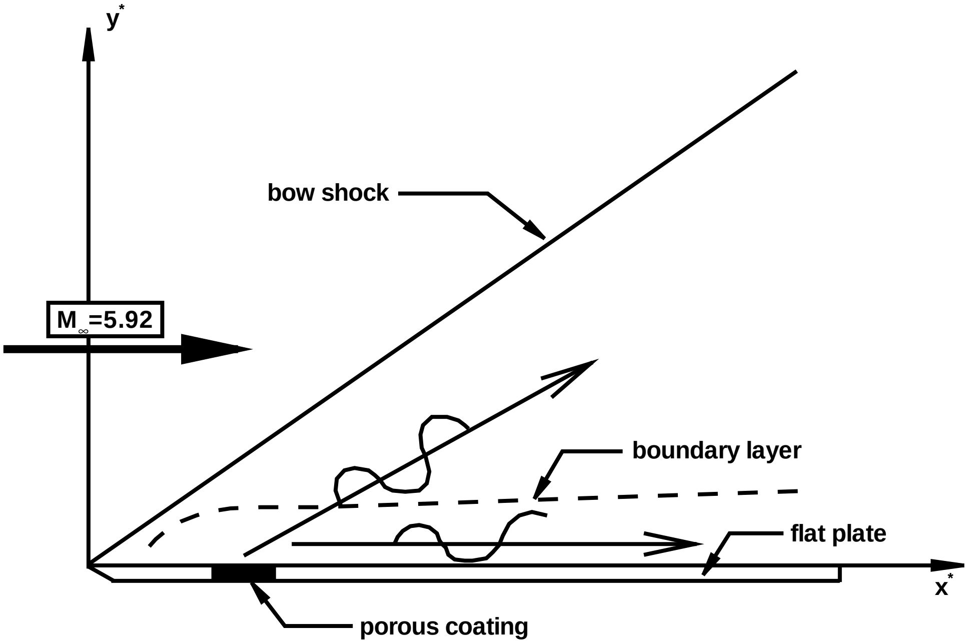

Figure 2: A schematic of the control of a Mach 5.92 flow over a flat plate with porous coating.

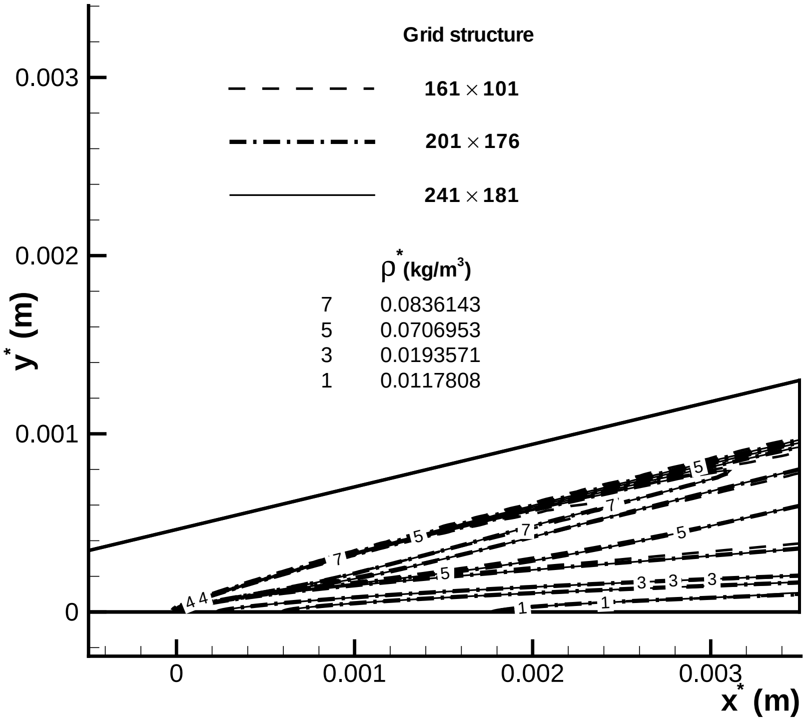

Figure 3: Comparison of density contours near the leading edge simulated by second-order TVD scheme based on three sets of grid structures.

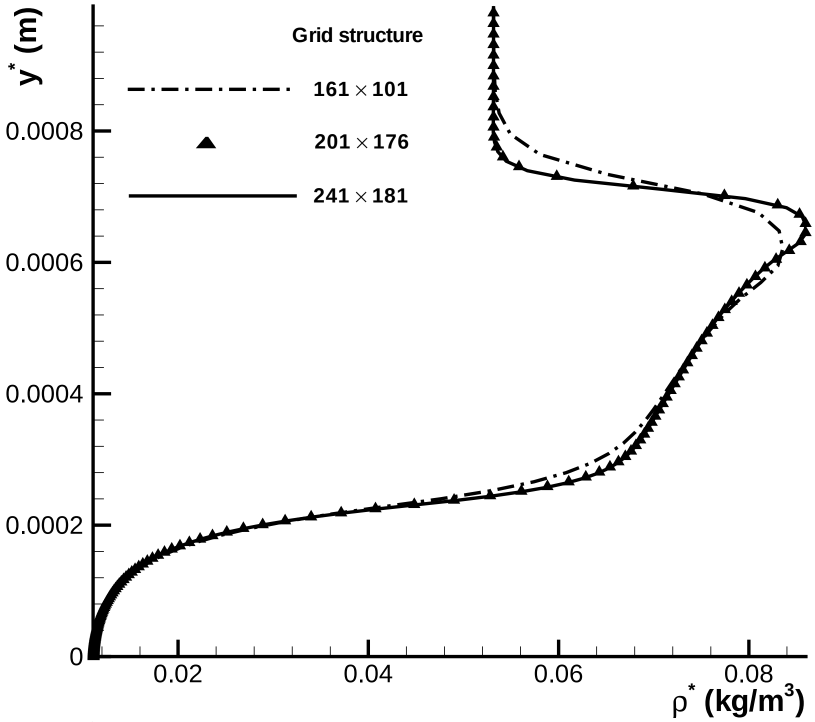

Figure 4: Comparison of density distributions in wall-normal direction at $x^* = 0.0025$ m simulated by second-order TVD scheme based on three sets of grid structures.

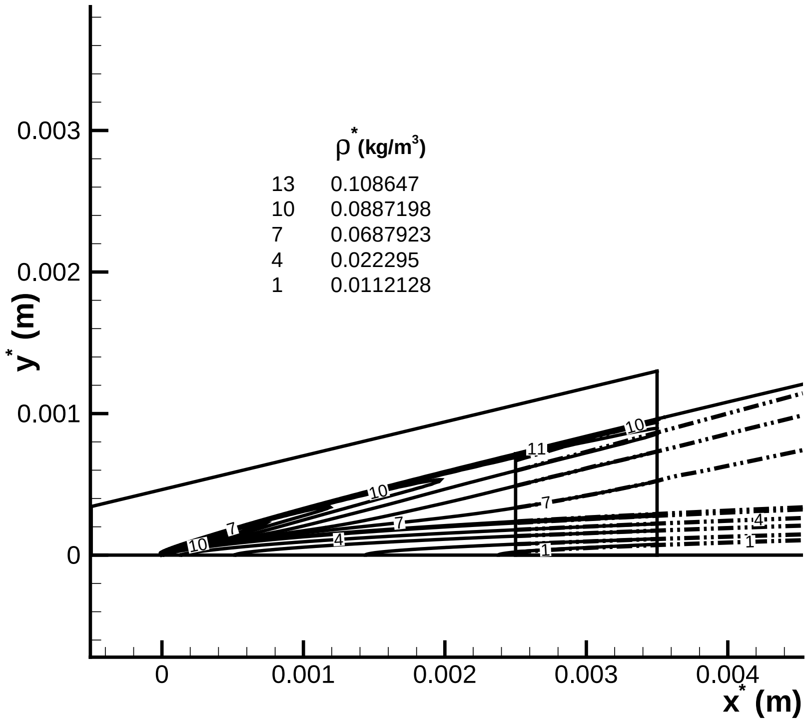

Figure 5: Density contours near the leading edge of the steady base flow obtained by the combination of second-order TVD scheme and fifth-order shock-fitting method.

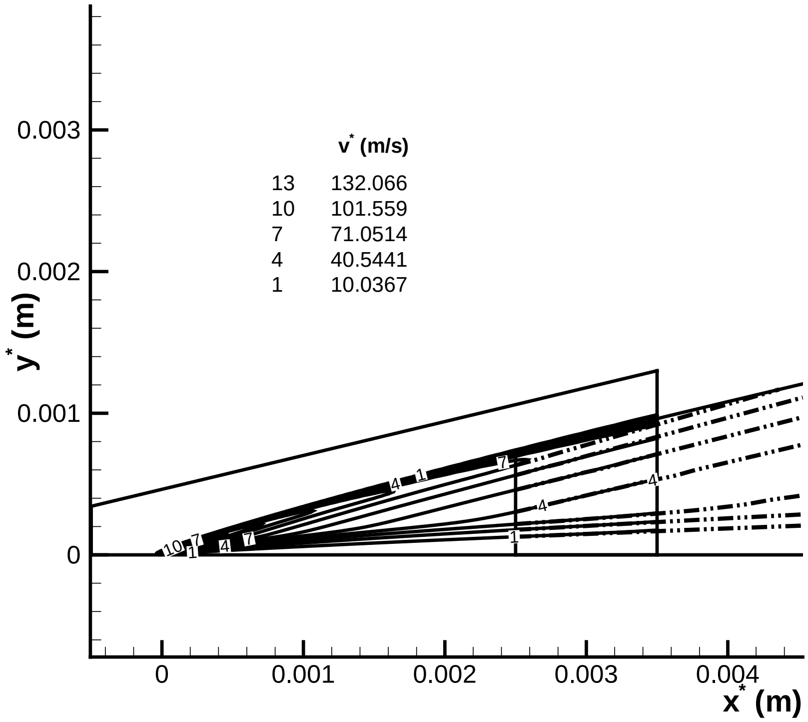

Figure 6: Wall-normal velocity contours near the leading edge of the steady base flow obtained by the combination of second-order TVD scheme and fifth-order shock-fitting method.

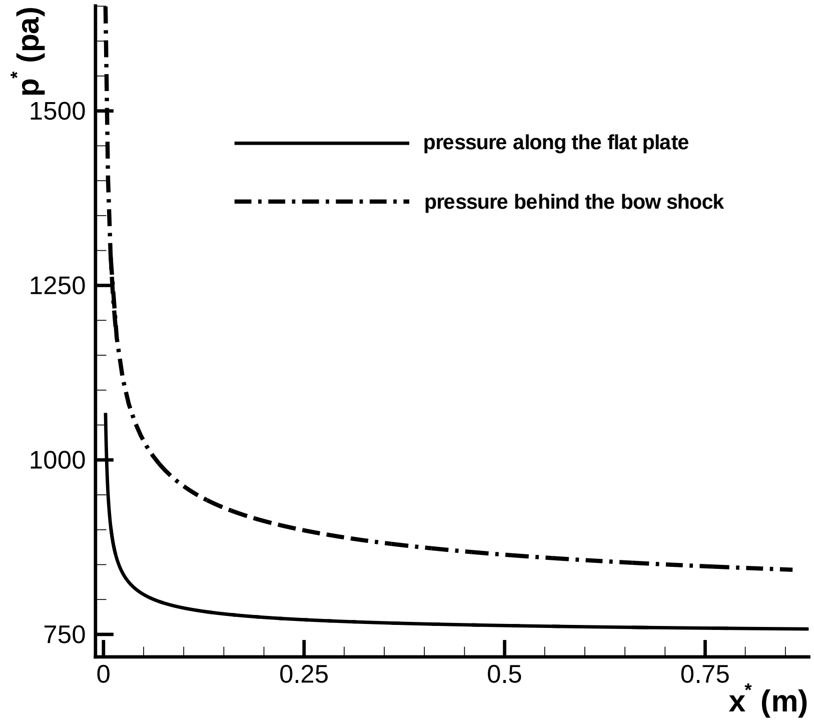

Figure 7: Pressure distributions along the flat plate and behind the shock of the steady base flow simulated by the fifth-order shock-fitting method.

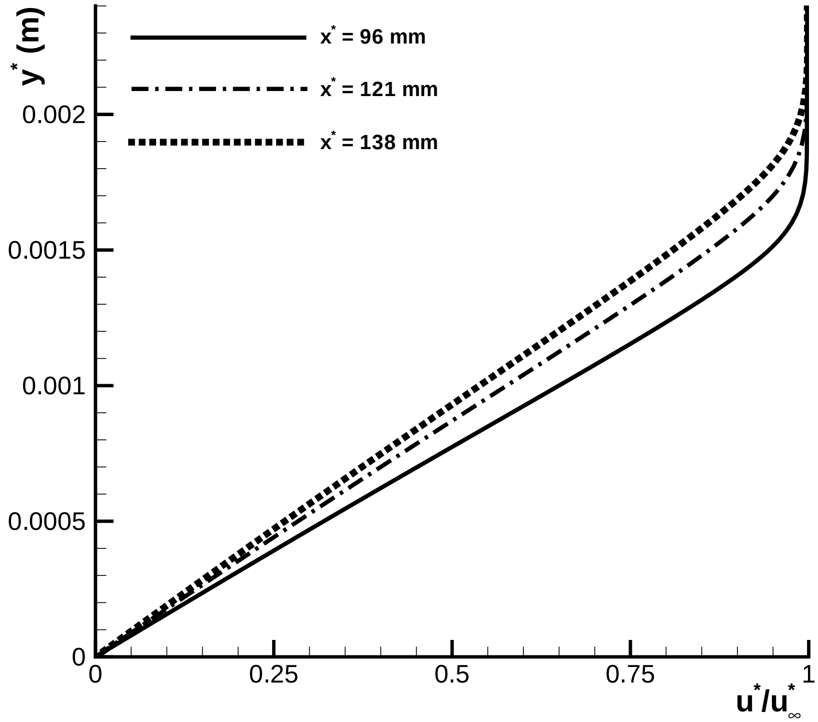

Figure 8: Distributions of dimensionless streamwise velocity across the boundary layer of the numerical steady base flow at three different locations.

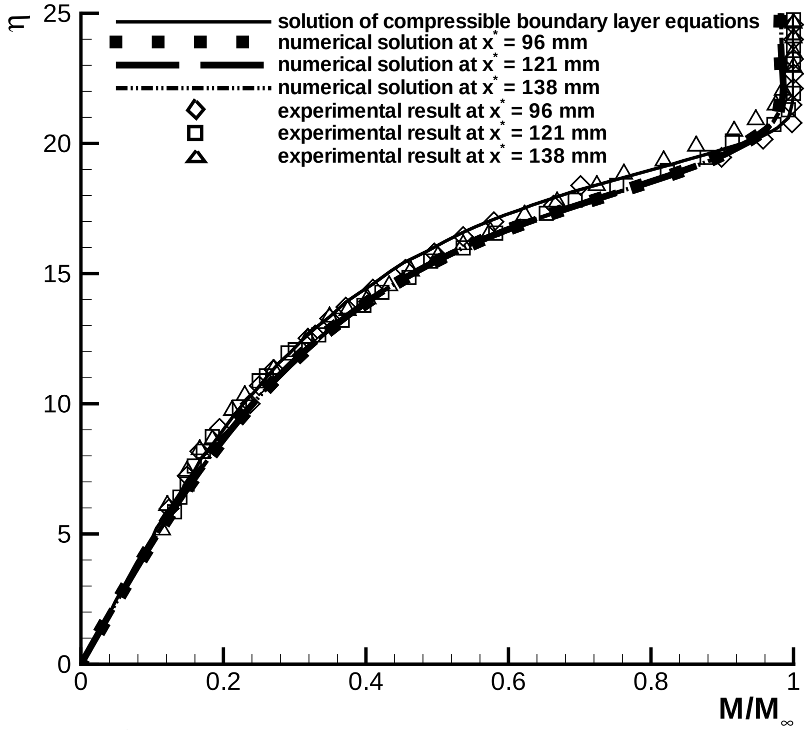

Figure 9: Comparison of normalized Mach number distributions across the boundary layer at three different locations.

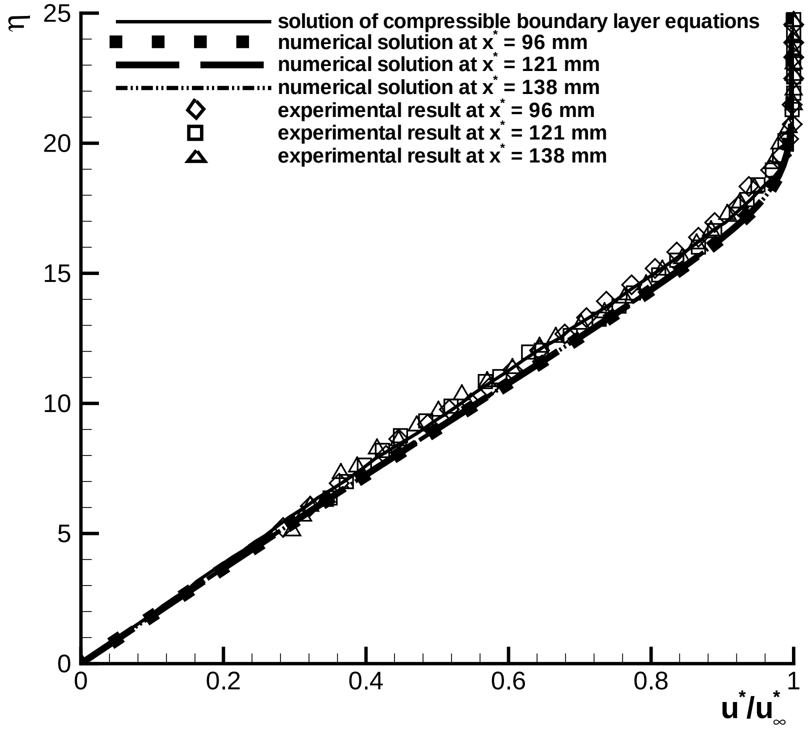

Figure 10: Comparison of dimensionless streamwise velocity distributions across the boundary layer at three different locations.

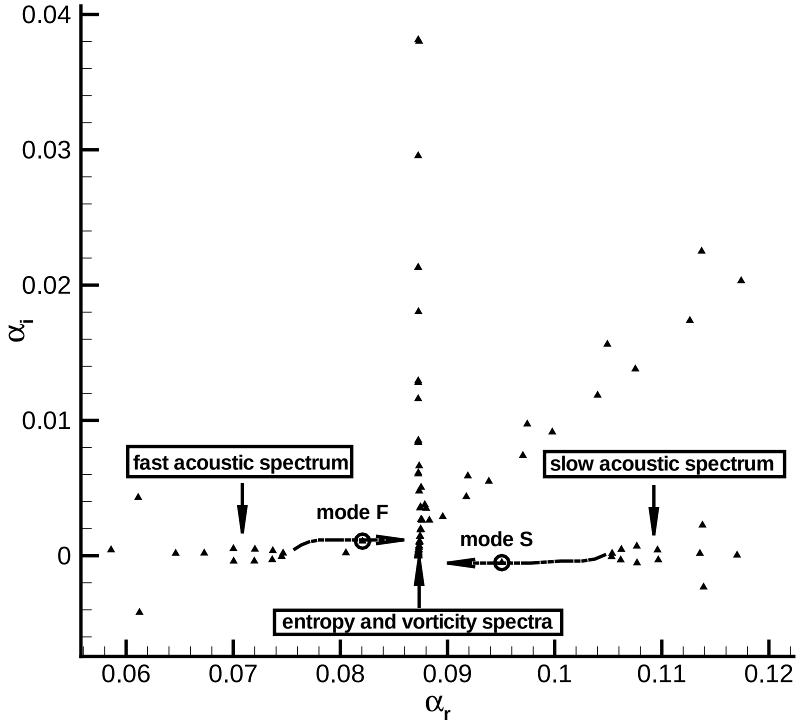

Figure 11: Eigenvalue spectra of the boundary-layer modes for a case at the frequency of $f^* = 100$ kHz at $x^* = 0.189$ m.

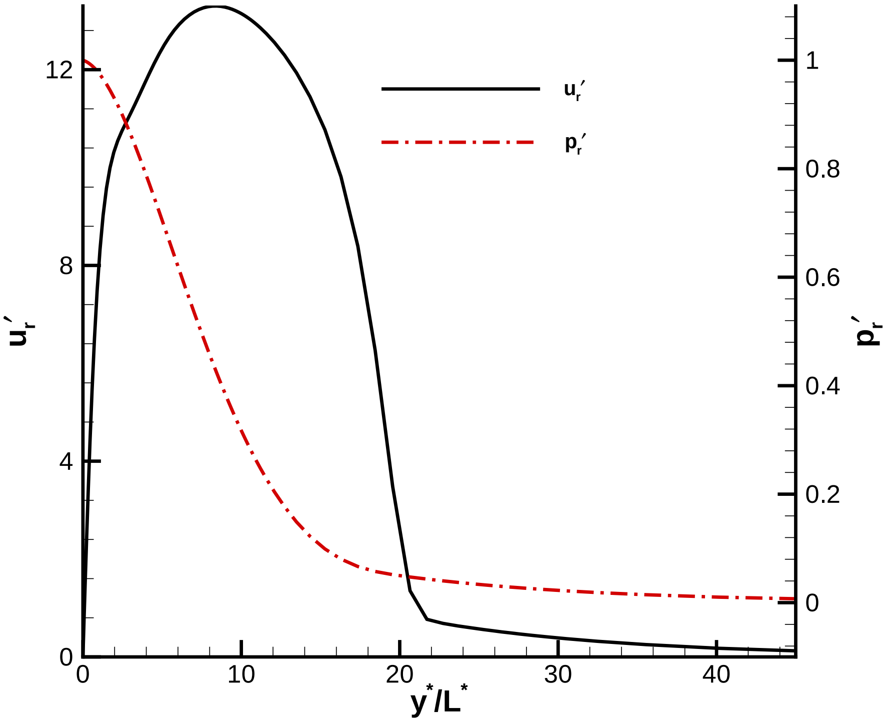

Figure 12: Eigenfunctions of streamwise velocity and pressure fluctuations of mode F at $x^* = 0.189$ m.

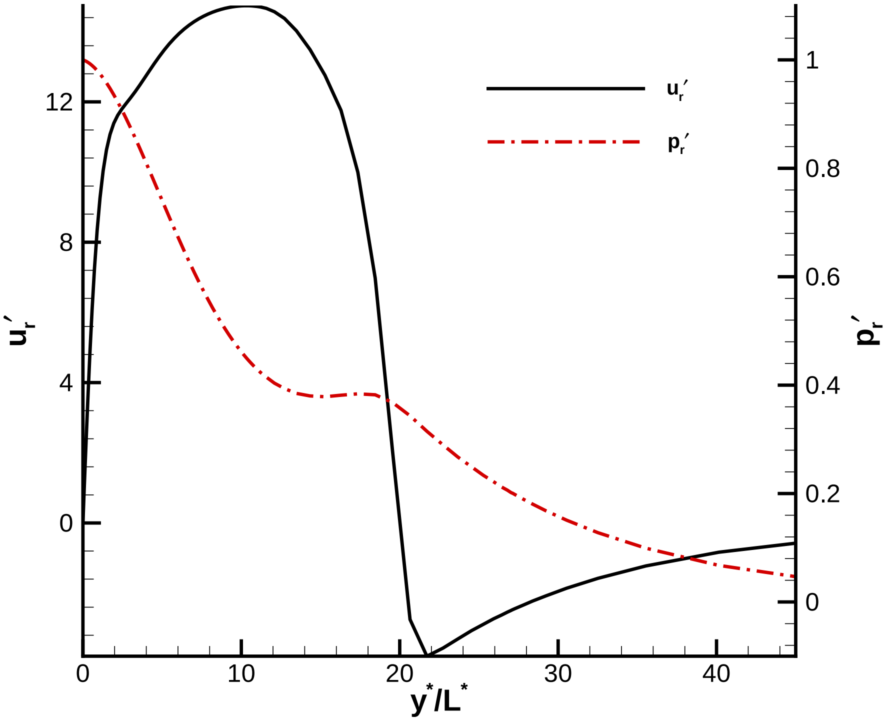

Figure 13: Eigenfunctions of streamwise velocity and pressure fluctuations of mode S at $x^* = 0.189$ m.

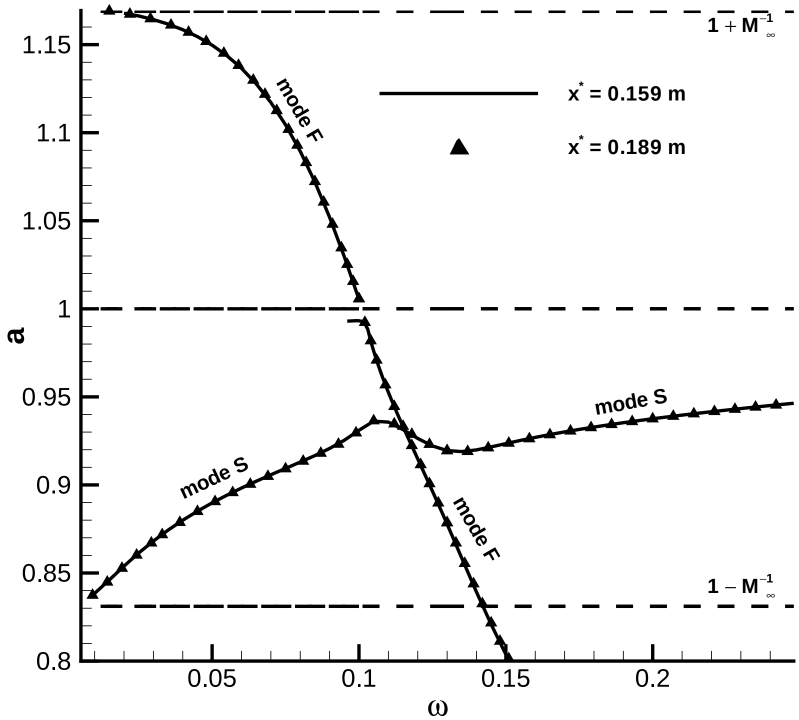

Figure 14: Distributions of dimensionless phase velocities of boundary-layer wave modes at two different locations versus dimensionless circular frequency.

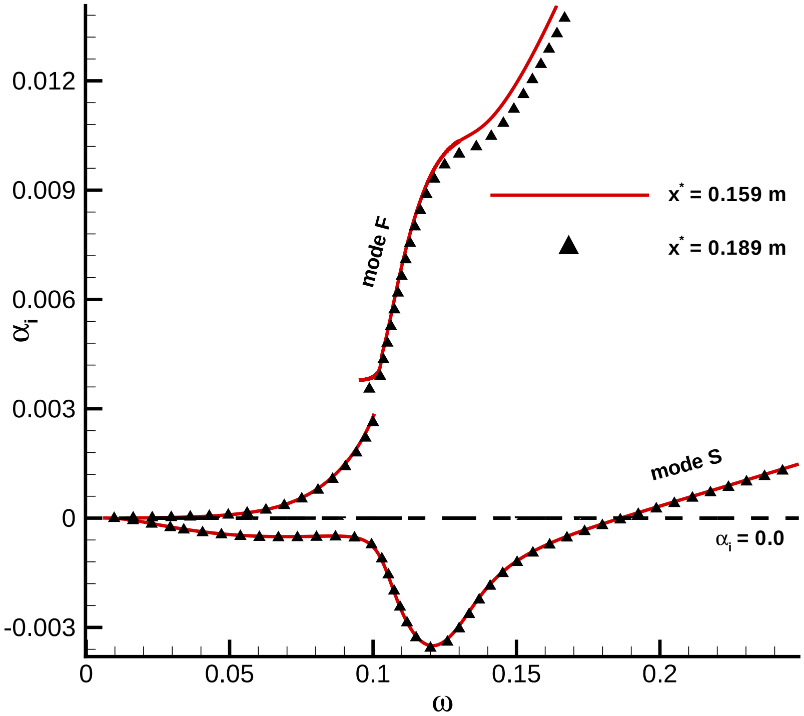

Figure 15: Distributions of growth rates of mode S and mode F at the two locations versus ω.

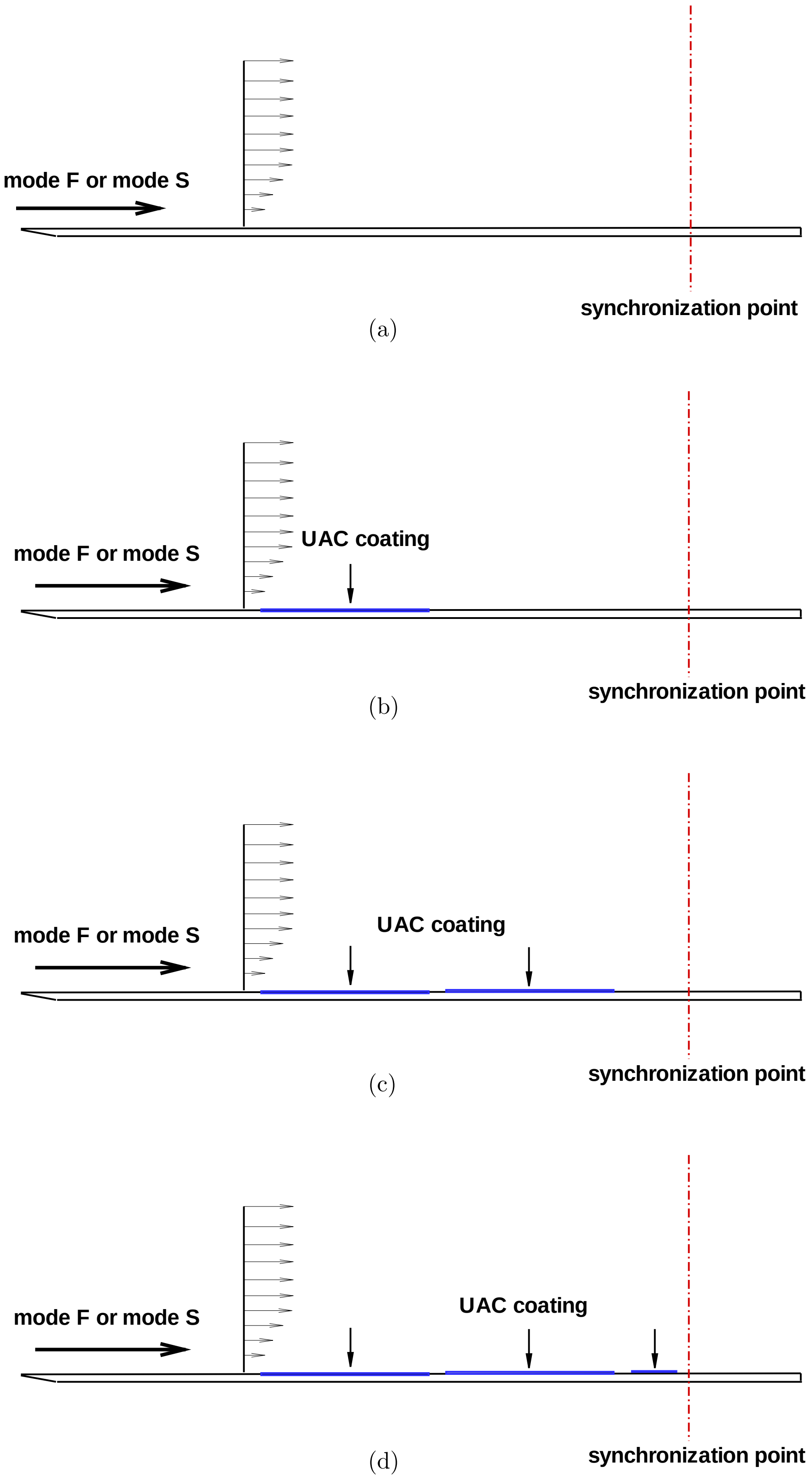

Figure 16: A schematic of porous coating locations and the synchronization point for the four cases of stability simulations: (a) case 1; (b) case 2; (c) case 3; (d) case 4.

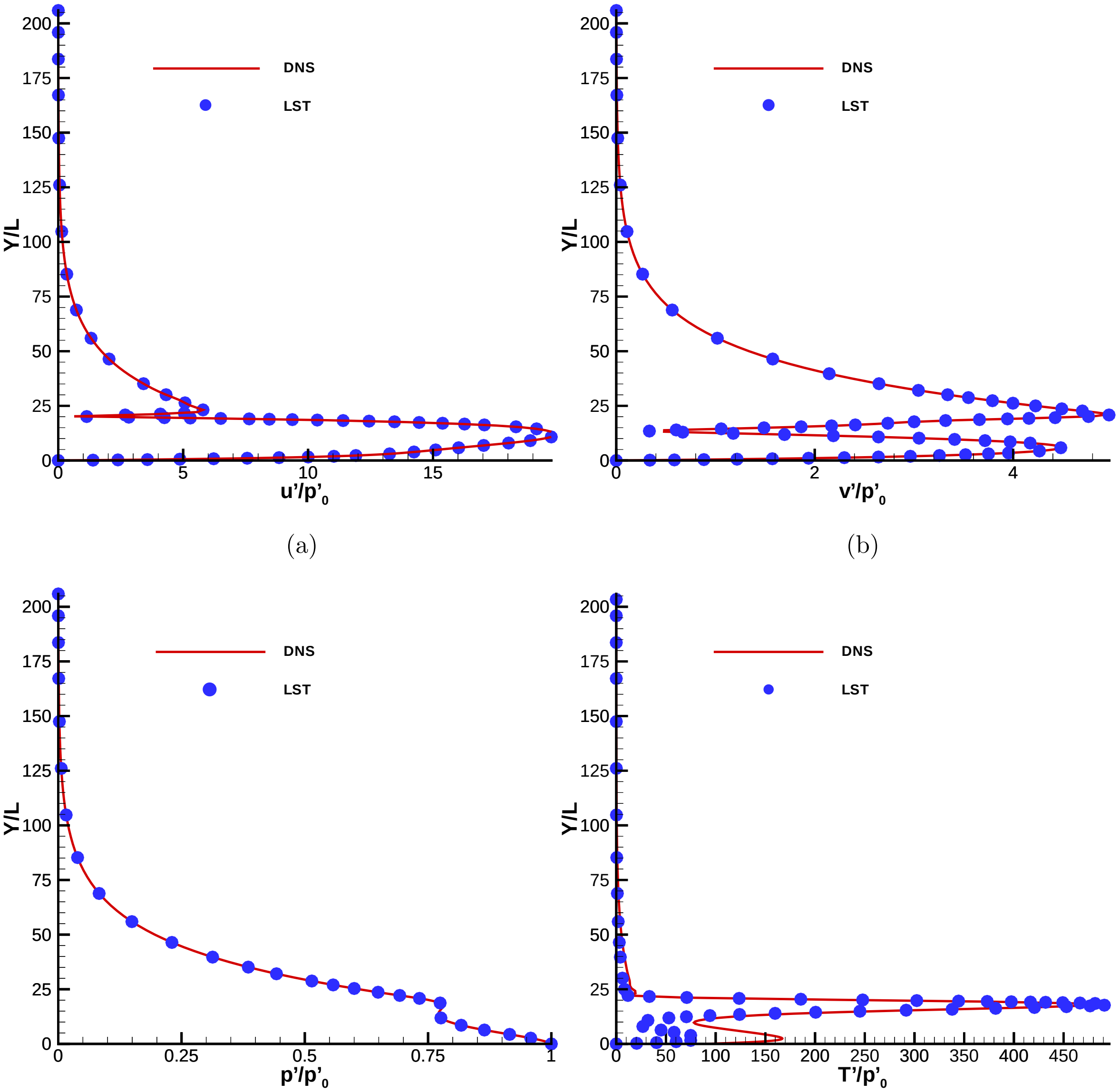

(a) (b)

(c) (d)

Figure 17: Comparisons of disturbance profiles introduced at the inlet with the eigenfunction of mode S obtained from LST: (a) streamwise velocity; (b) wall-normal velocity; (c) pressure; (d) temperature.

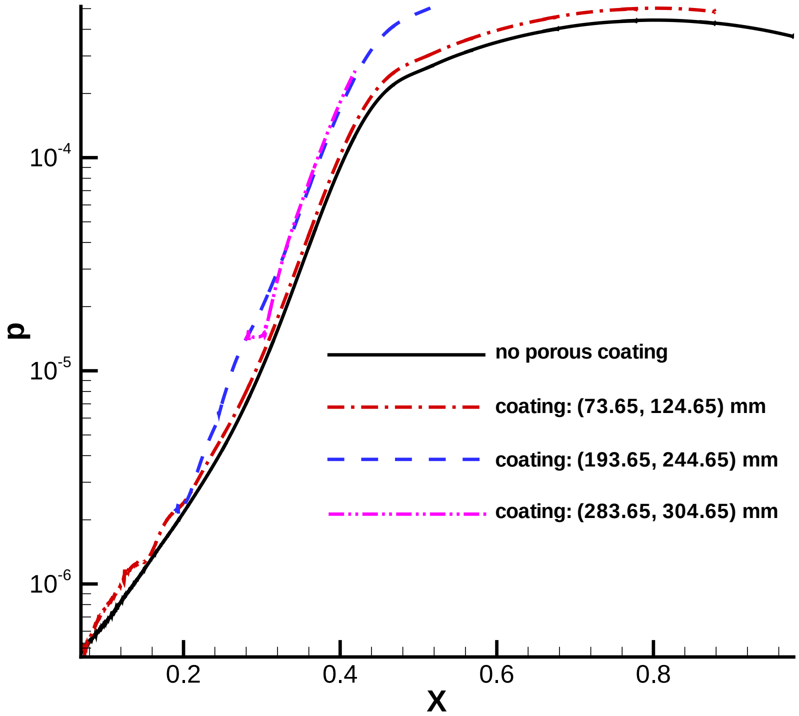

Figure 18: Amplitude distributions of pressure perturbation along the flat plate for the four cases of stability simulations.

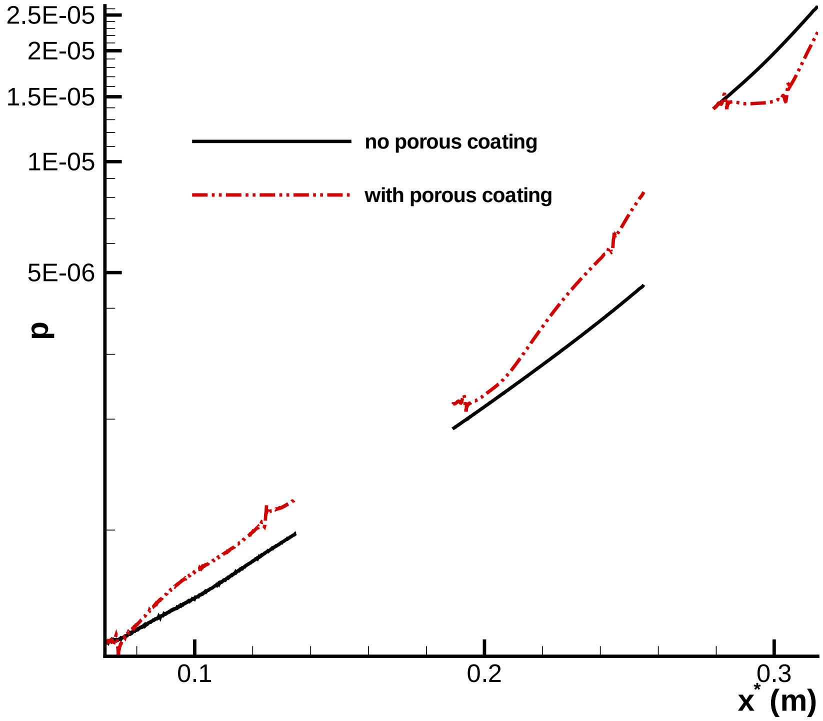

Figure 19: Comparison of pressure perturbation amplitude obtained from numerical simulation with porous coating with that obtained from numerical simulation without porous coating.

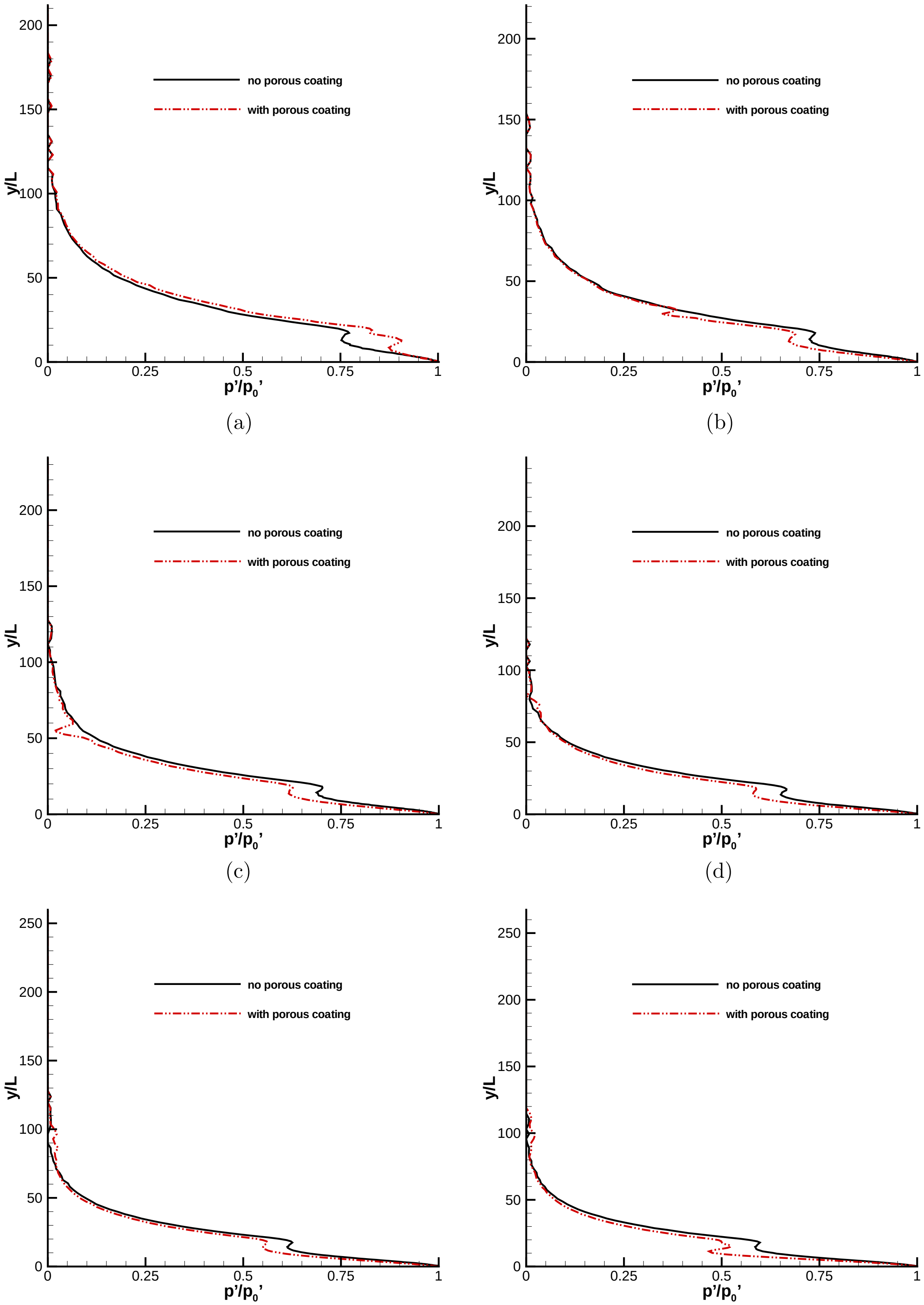

(a) (b) (c) (d) (e) (f)

Figure 20: Comparisons of normalized pressure perturbation amplitudes obtained from numerical simulations with/without porous coating at six locations in the region $(73.65, 124.65)$ mm: (a) 73.65 mm; (b) 81.00 mm; (c) 93.00 mm; (d) 105.00 mm; (e) 117.00 mm; (f) 124.65 mm.

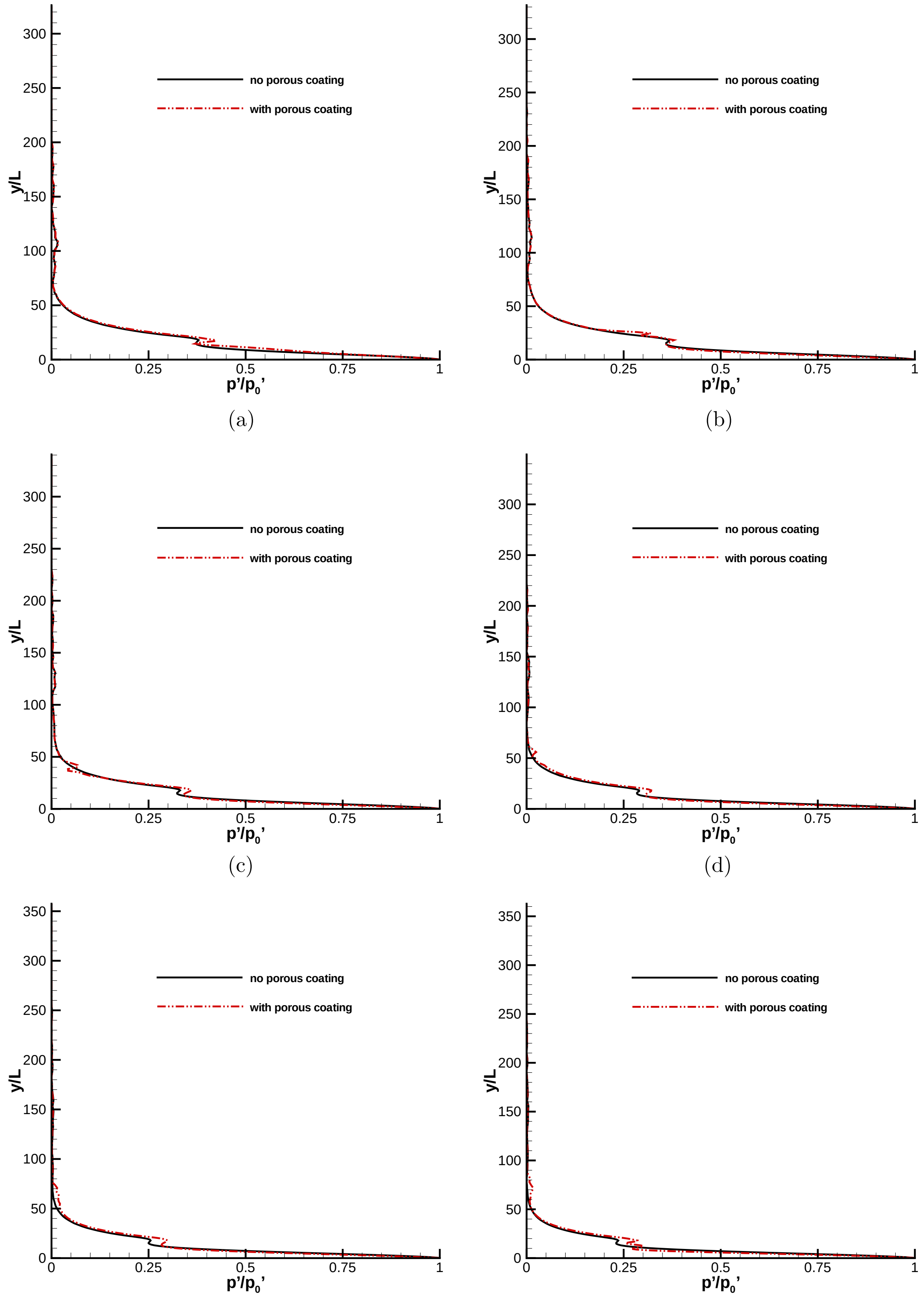

(a) (b)

(c) (d)

(e) (f)

Figure 21: Comparisons of normalized pressure perturbation amplitudes obtained from numerical simulations with/without porous coating at six locations in the region $(193.65, 244.65)$ mm: (a) 193.65 mm; (b) 201.00 mm; (c) 213.00 mm; (d) 225.00 mm; (e) 237.00 mm; (f) 244.65 mm.

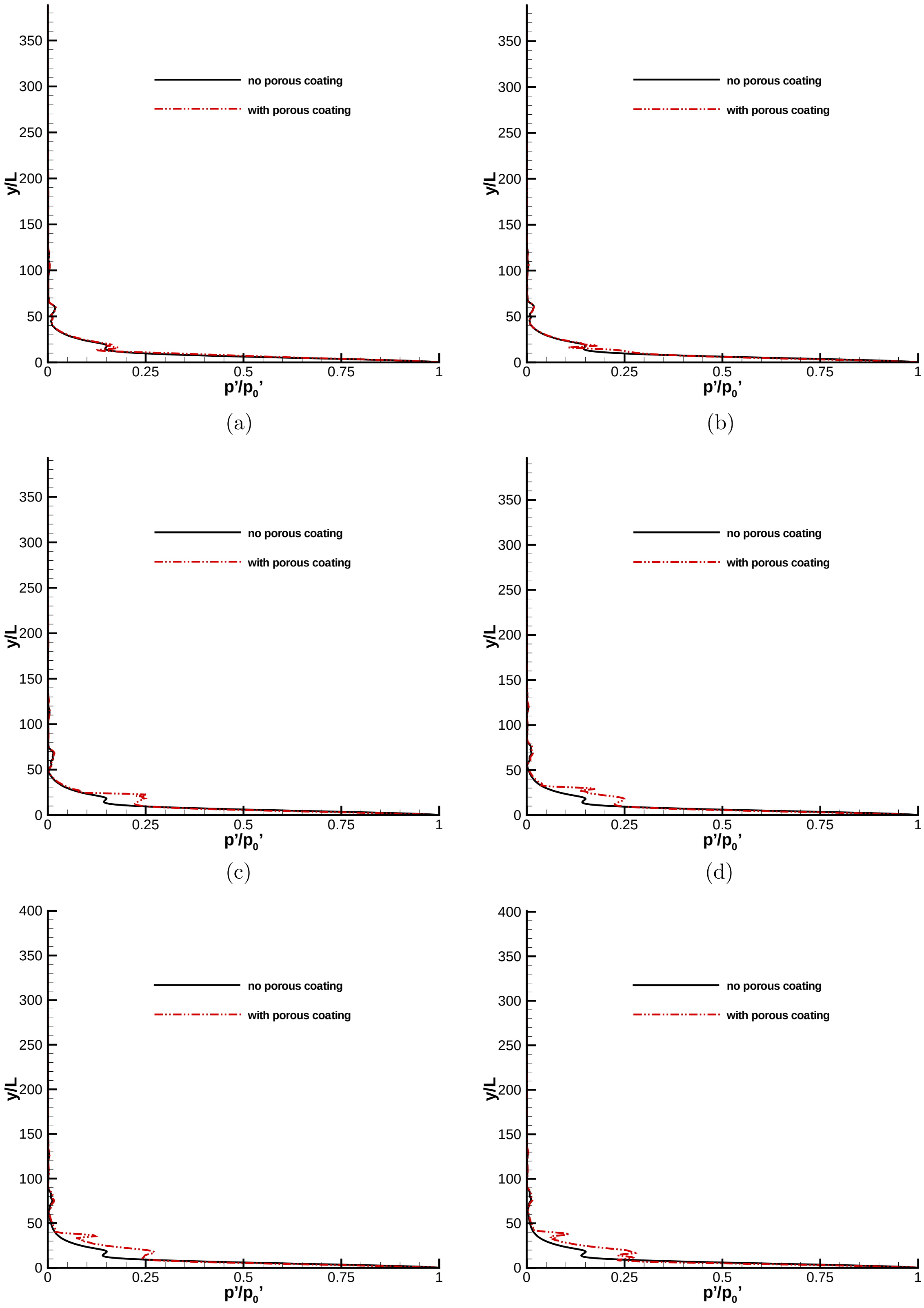

(a) (b) (c) (d) (e) (f)

Figure 22: Comparisons of normalized pressure perturbation amplitudes obtained from numerical simulations with/without porous coating at six locations in the region $(283.65, 304.65)$ mm: (a) 283.65 mm; (b) 285.00 mm; (c) 291.00 mm; (d) 297.00 mm; (e) 303.00 mm; (f) 304.65 mm.

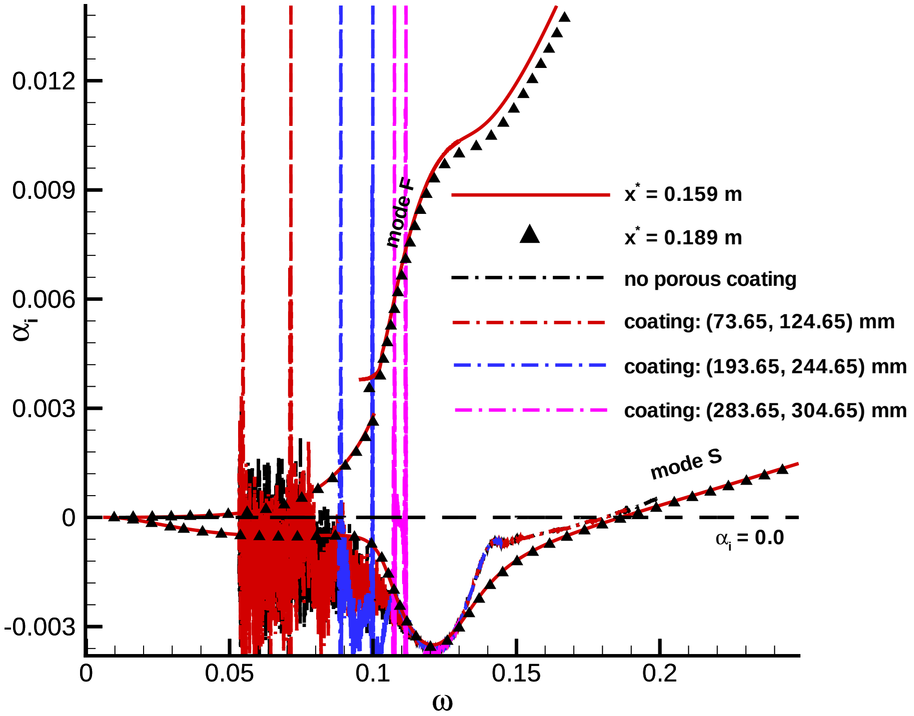

Figure 23: Comparison of the growth rate calculated from numerical simulation results with that obtained from LST for the four cases of stability simulations.

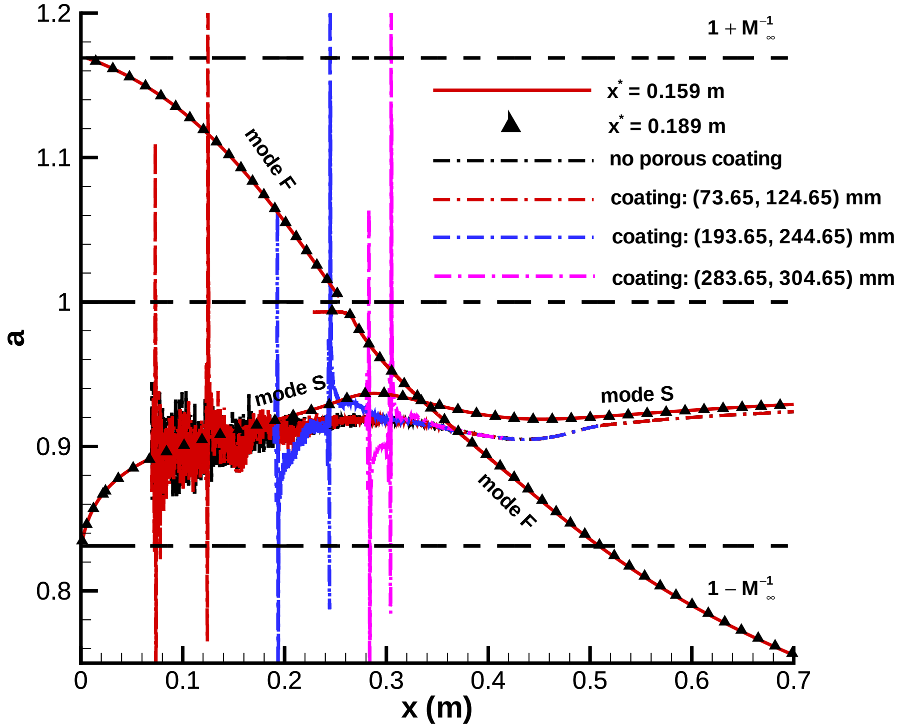

Figure 24: Comparison of the phase velocity calculated from numerical simulation results with that obtained from LST for the four cases of stability simulations.

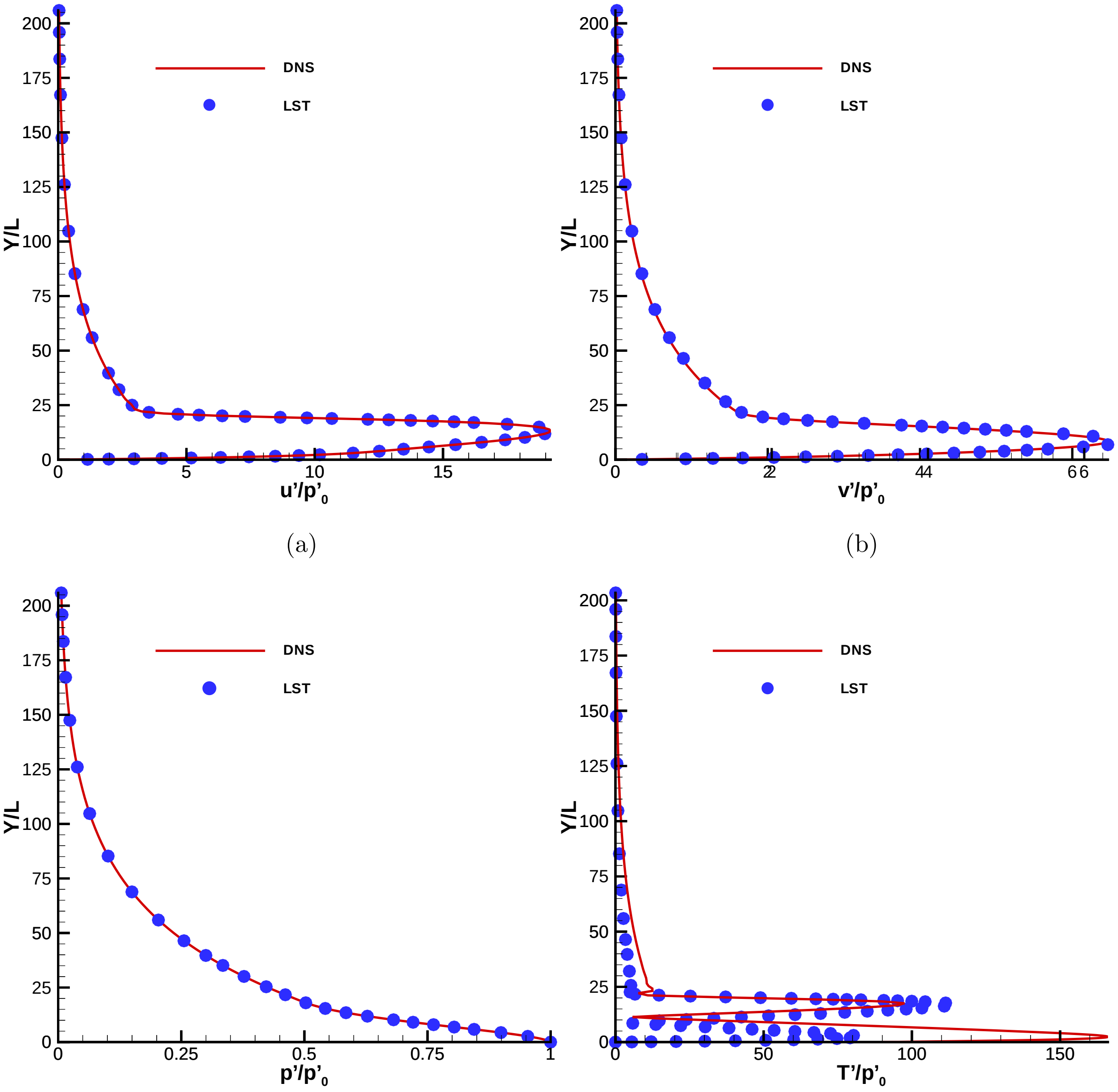

(a) (b)

(c) (d)

Figure 25: Comparisons of disturbance profiles introduced at the inlet with the eigenfunction of mode F obtained from LST: (a) streamwise velocity; (b) wall-normal velocity; (c) pressure; (d) temperature.

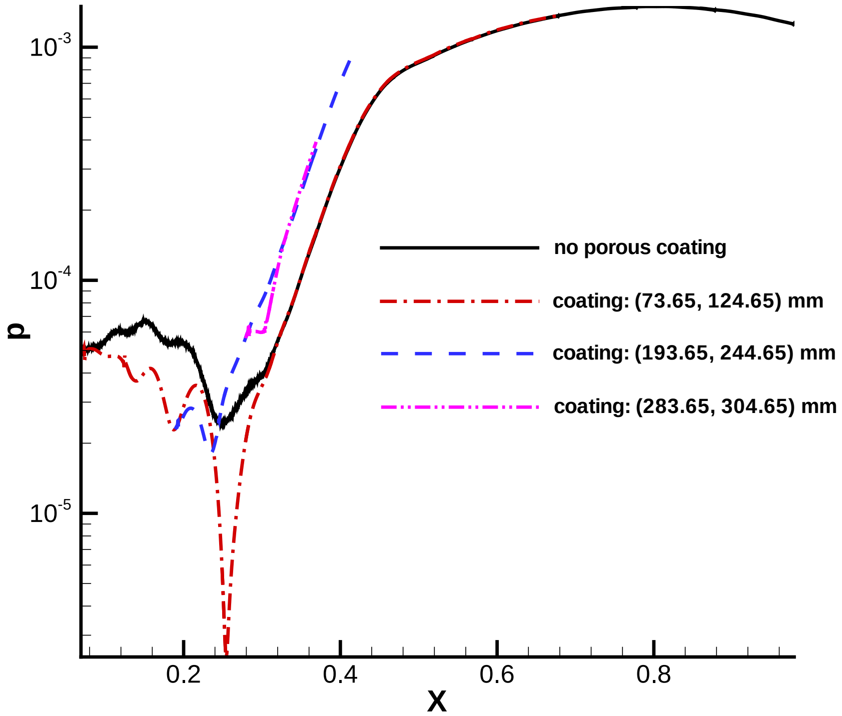

Figure 26: Amplitude distributions of pressure perturbation along the flat plate for the four cases of stability simulations.

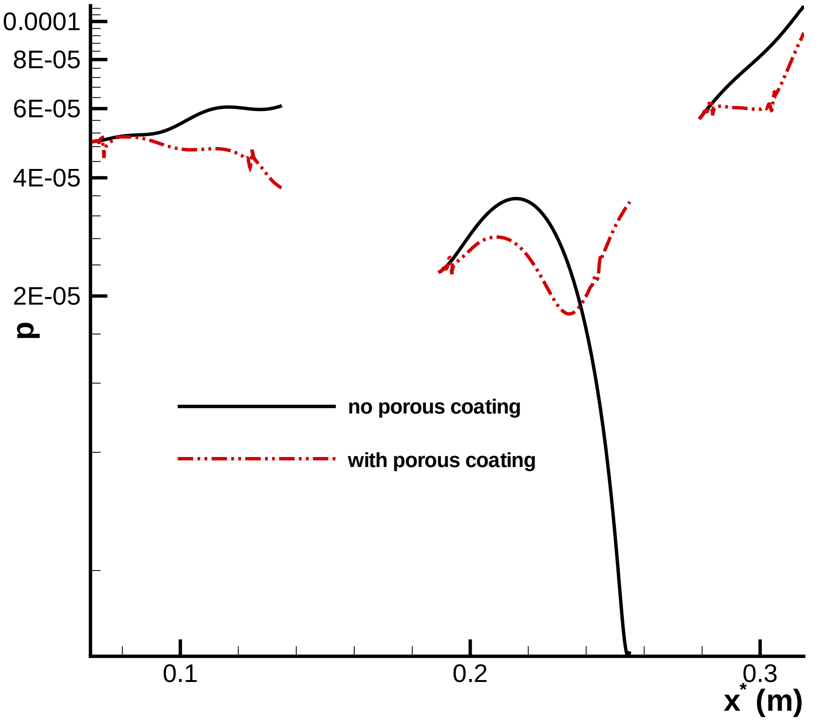

Figure 27: Comparison of pressure perturbation amplitude obtained from numerical simulation with porous coating with that obtained from numerical simulation without porous coating.

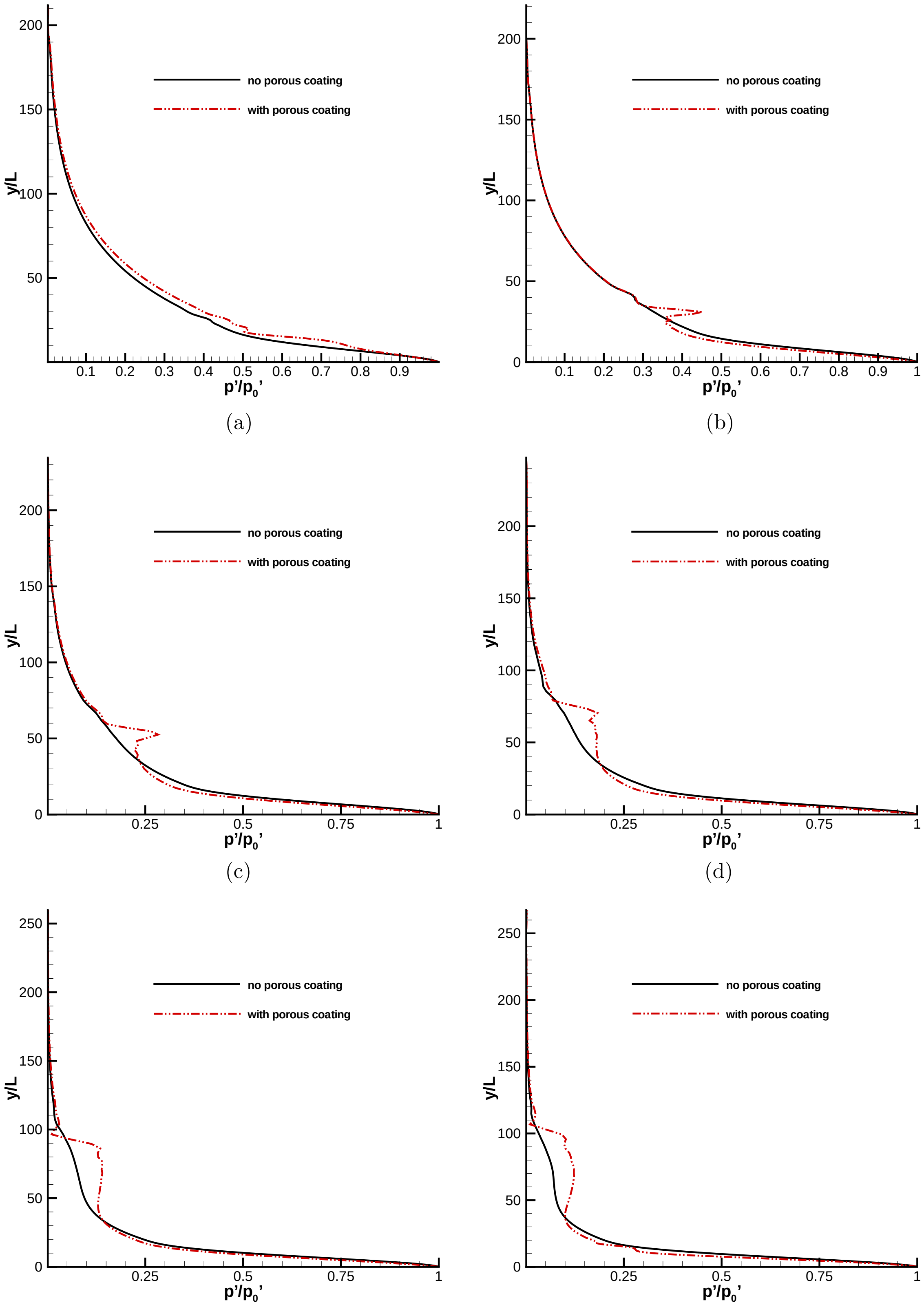

(a) (b) (c) (d) (e) (f)

Figure 28: Comparisons of normalized pressure perturbation amplitudes obtained from numerical simulations with/without porous coating at six locations in the region $(73.65, 124.65)$ mm: (a) 73.65 mm; (b) 81.00 mm; (c) 93.00 mm; (d) 105.00 mm; (e) 117.00 mm; (f) 124.65 mm.

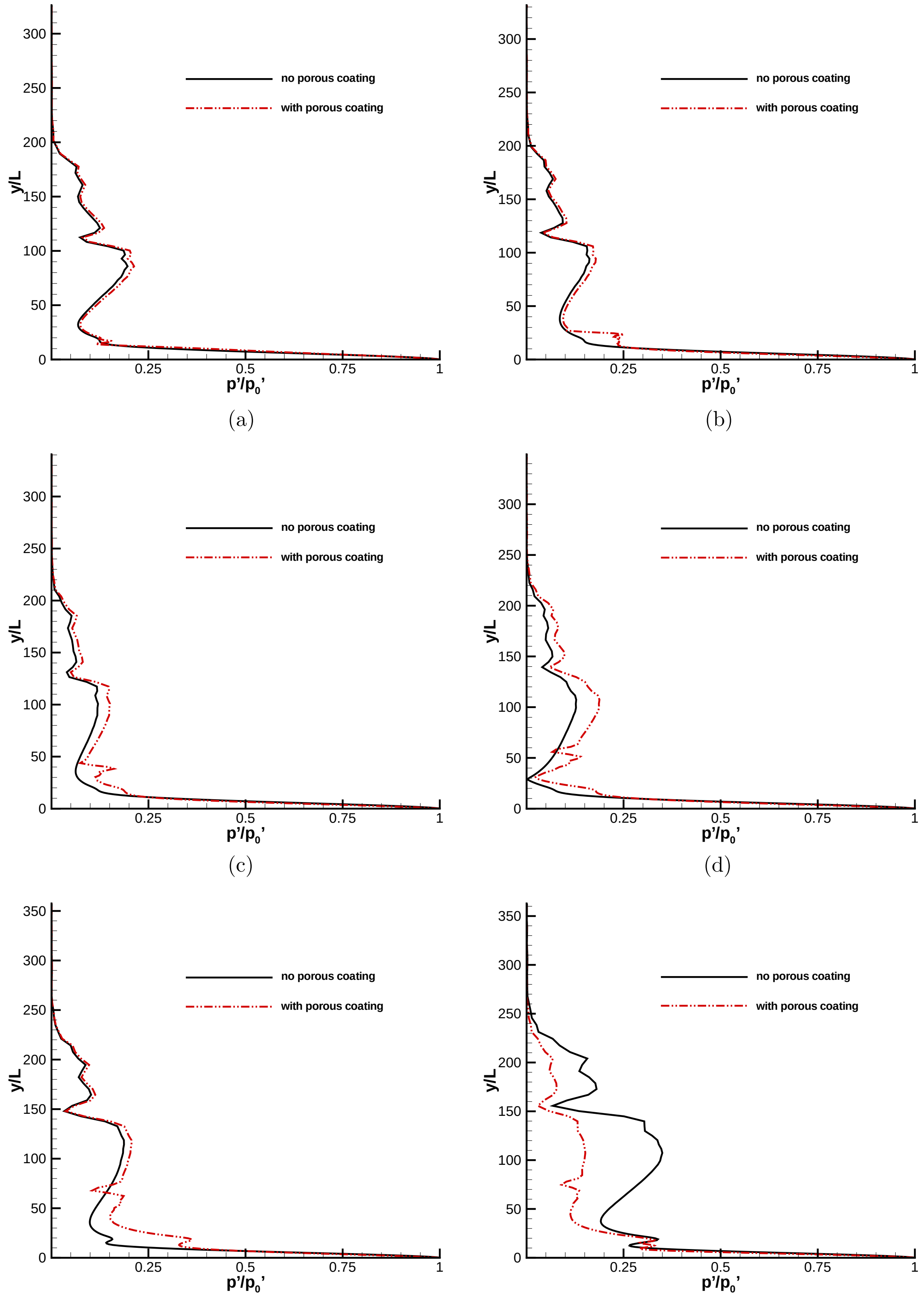

(a) (b) (c) (d) (e) (f)

Figure 29: Comparisons of normalized pressure perturbation amplitudes obtained from numerical simulations with/without porous coating at six locations in the region $(193.65, 244.65)$ mm: (a) 193.65 mm; (b) 201.00 mm; (c) 213.00 mm; (d) 225.00 mm; (e) 237.00 mm; (f) 244.65 mm.

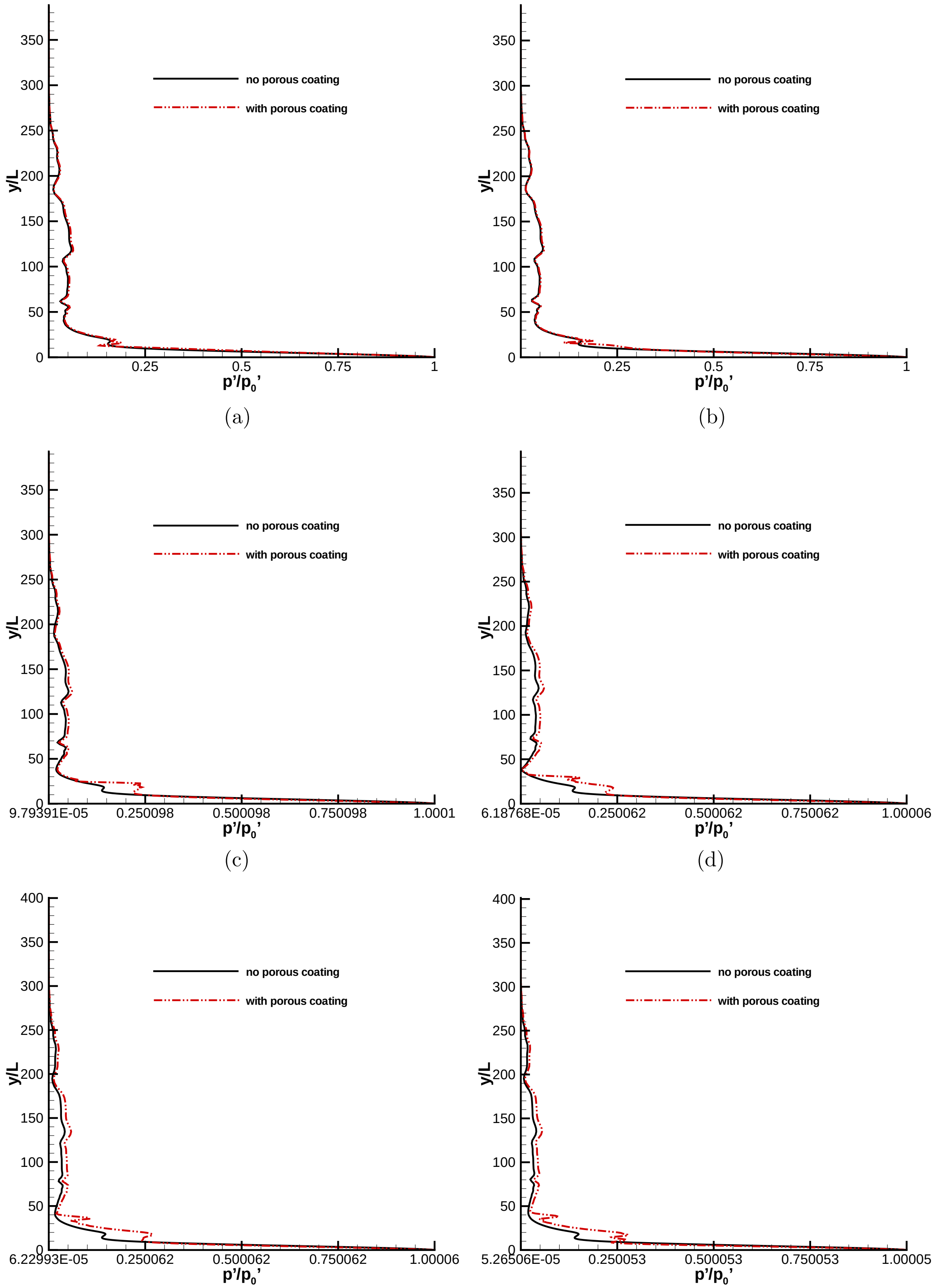

(a) (b)

(c) (d)

(e) (f)

Figure 30: Comparisons of normalized pressure perturbation amplitudes obtained from numerical simulations with/without porous coating at six locations in the region $(283.65, 304.65)$ mm: (a) 283.65 mm; (b) 285.00 mm; (c) 291.00 mm; (d) 297.00 mm; (e) 303.00 mm; (f) 304.65 mm.

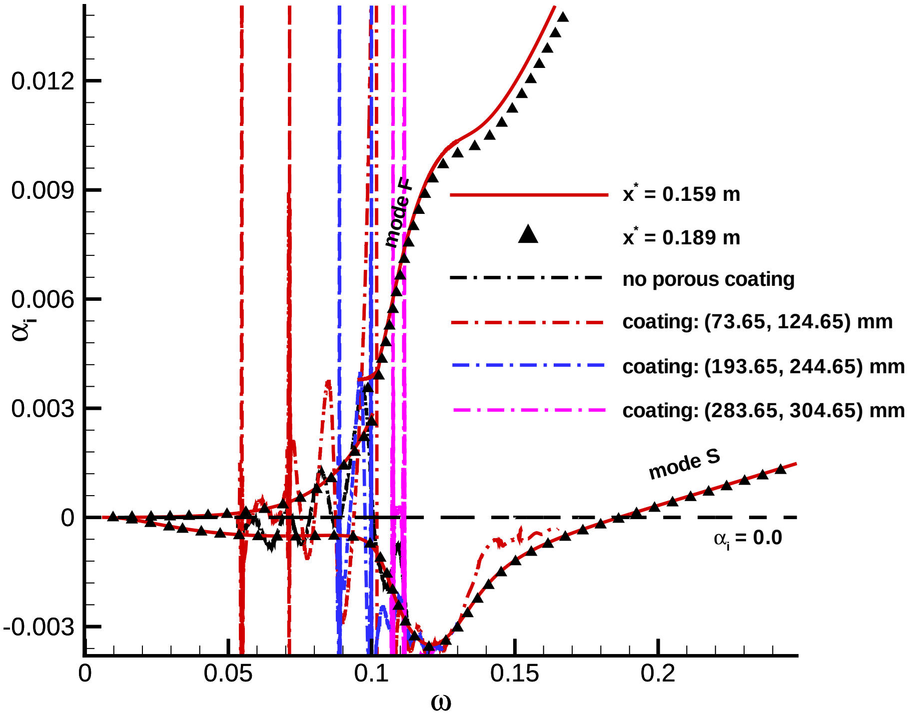

Figure 31: Comparison of the growth rate calculated from numerical simulation results with that obtained from LST for the four cases of stability simulations.

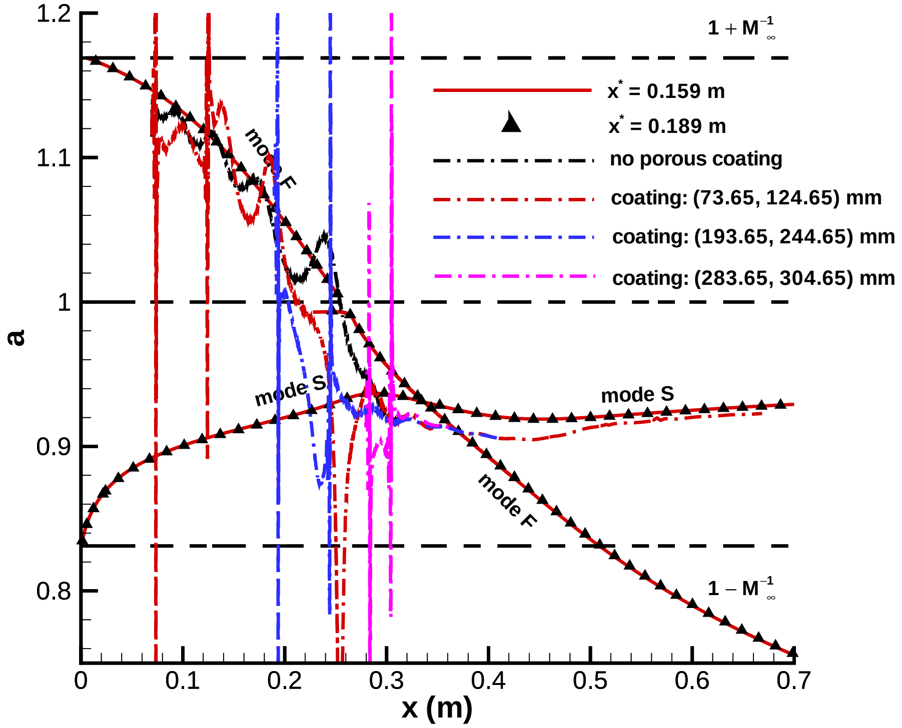

Figure 32: Comparison of the phase velocity calculated from numerical simulation results with that obtained from LST for the four cases of stability simulations.